*Communications in Applied Mathematics and Computational Science*

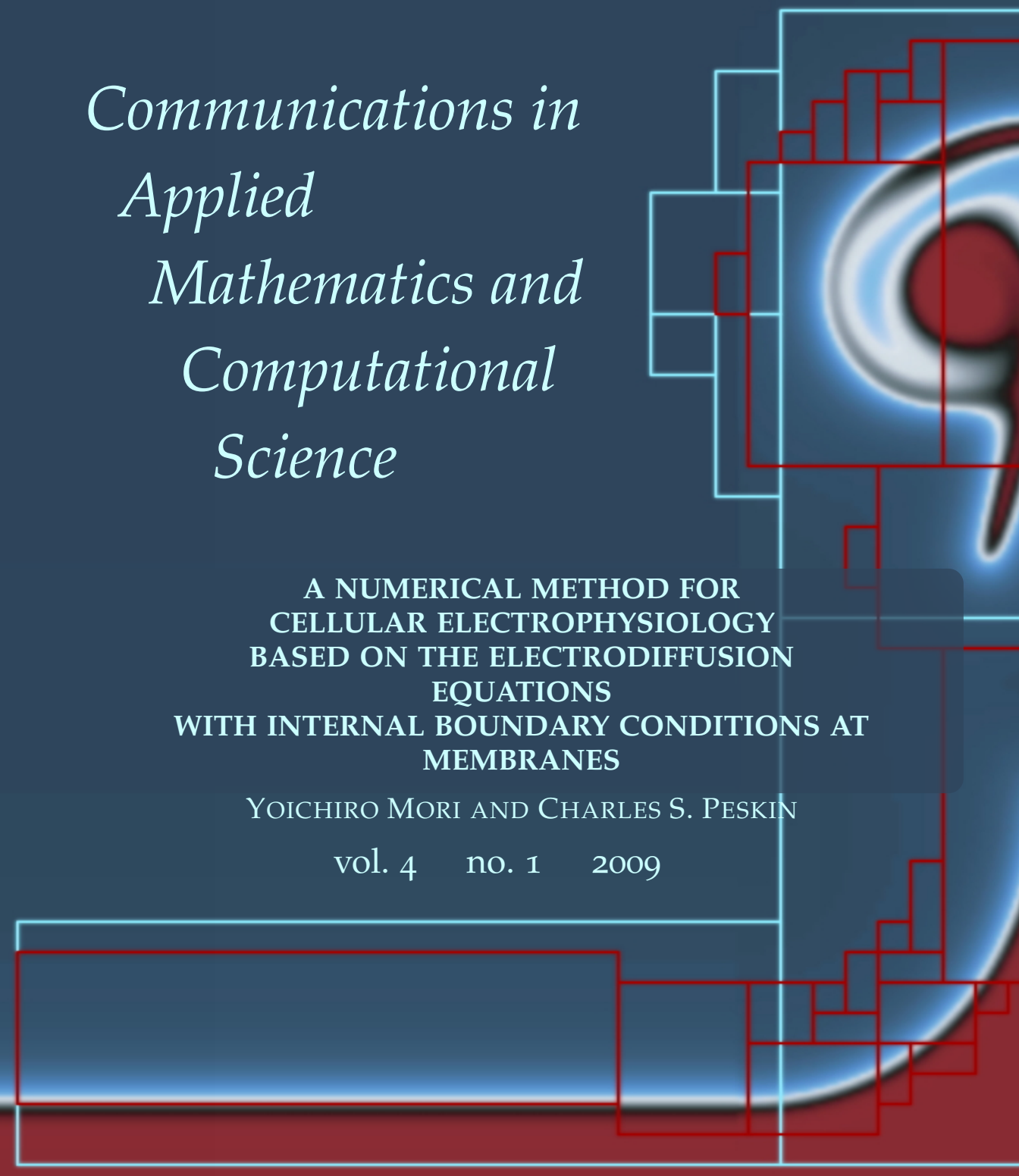

# A NUMERICAL METHOD FOR CELLULAR ELECTROPHYSIOLOGY BASED ON THE ELECTRODIFFUSION EQUATIONS WITH INTERNAL BOUNDARY CONDITIONS AT MEMBRANES

YOICHIRO MORI AND CHARLES S. PESKIN

vol. 4 no. 1 2009

mathematical sciences publishers

COMM. APP. MATH. AND COMP. SCI.
Vol. 4, No. 1, 2009

# A NUMERICAL METHOD FOR CELLULAR ELECTROPHYSIOLOGY BASED ON THE ELECTRODIFFUSION EQUATIONS WITH INTERNAL BOUNDARY CONDITIONS AT MEMBRANES

YOICHIRO MORI AND CHARLES S. PESKIN

We present a numerical method for solving the system of equations of a model of cellular electrical activity that takes into account both geometrical effects and ionic concentration dynamics. A challenge in constructing a numerical scheme for this model is that its equations are stiff: There is a time scale associated with "diffusion" of the membrane potential that is much faster than the time scale associated with the physical diffusion of ions. We use an implicit discretization in time and a finite volume discretization in space. We present convergence studies of the numerical method for cylindrical and two-dimensional geometries for several cases of physiological interest.

## 1. Introduction

Cellular electrical activity is central to cellular physiology [1], and it has been an area in which mathematical modeling has seen great success [16; 18]. Most models of cellular electrical activity are based on the cable model, in which an ohmic current continuity relation results in a one-dimensional reaction diffusion system [16; 18].

In the derivation of the cable model, one assumes that the ionic concentrations do not change appreciably over the time of interest, and that a one-dimensional picture of cell geometry is adequate for purposes of describing cellular electrical activity. In [25; 27], we presented a three-dimensional model of cellular electrical activity that takes into account both ionic concentration and geometrical effects on electrophysiology. The resulting system of partial differential equations has the virtue of being more general in its physiological applicability, but has the difficulty of being far more complicated to study either analytically or numerically.

In this paper, we develop an efficient numerical method to solve this system of equations in two spatial dimensions. In Section 2, we give a short presentation of

*MSC2000:* 65M12, 92C30, 92C50.

*Keywords:* three-dimensional cellular electrophysiology, electrodiffusion, ephaptic transmission, finite volume method.

the model equations and in Section 3 we discuss the time and space scales that are relevant to the behavior of the model. We shall see that the model equations have two time scales of interest, the ionic diffusion time scale and the membrane potential time scale. The membrane potential time scale is associated with the "diffusion" of the membrane potential, which is closely related to the spread of the membrane potential in the cable model. In Section 4, we discuss spatial discretization. We use a finite volume scheme and develop a numerical scheme for cylindrical geometry and a related scheme for arbitrary two-dimensional geometry. In Section 5, we discuss time discretization. We use an operator splitting approach. Each time step is split into two substeps, one in which the gating variables are updated and the other in which the electrostatic potential and the ionic concentrations are updated. For the latter substep, a the electrostatic potential and ionic concentrations are treated implicitly to deal with the disparity of time scales mentioned above. We then discuss the iterative numerical solution of the nonlinear algebraic equations which result from the discretization. We conclude with convergence studies using several examples of biophysical relevance: the Hodgkin–Huxley axon, ephaptic transmission between cardiac cells, and three model geometries at length scales typically found in the central nervous system.

## 2. Model equations

We consider biological tissue to be a three-dimensional space partitioned into the intracellular and extracellular spaces by membranes. In these regions, we track the ionic concentrations as well as the electrostatic potential. Let the biological tissue of interest be divided into membrane bound subregions $\Omega^{(k)}$, indexed by $k$. We denote the membrane separating the regions $\Omega^{(k)}$ and $\Omega^{(l)}$ by $\Gamma^{(kl)}$ (Figure 1).

In any of the subregions $\Omega^{(k)}$, both the extracellular and intracellular, the equations satisfied by the ionic concentrations $c_i$ and the electrostatic potential $\phi$ are

$$\frac{\partial c_i}{\partial t} = -\nabla \cdot \boldsymbol{f}_i, \qquad \text{(ion conservation)} \tag{1}$$

$$\boldsymbol{f}_i = -D_i\left(\nabla c_i + \frac{q z_i c_i}{k_B T}\nabla\phi\right), \qquad \text{(drift-diffusion flux)} \tag{2}$$

$$0 = \rho_0 + \sum_{i=1}^{N} q z_i c_i, \qquad \text{(electroneutrality condition).} \tag{3}$$

Here, $\boldsymbol{f}_i$ denotes the flux of the $i$-th species of ion. This quantity is expressed as a sum of a diffusion term and a drift term. $D_i$ is the diffusion coefficient of the $i$-th ion, $qz_i$ is the amount of charge on the $i$-th ion, where $q$ is the proton charge. Thus $qD_i/(k_BT)$ is the mobility of the ion species (Einstein relation), where $k_B$ is the

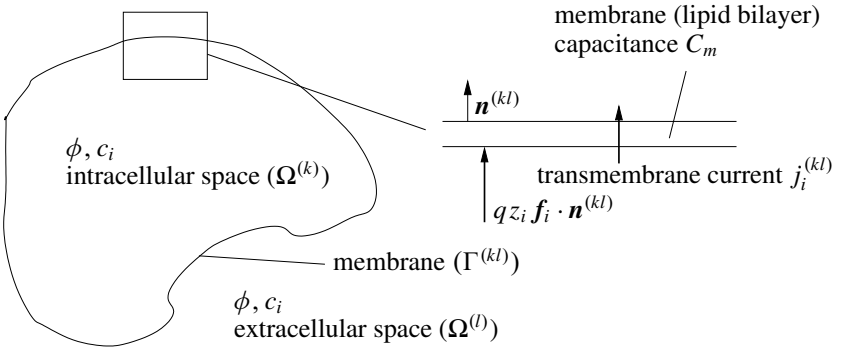


**Figure 1.** The variables $\phi, c_i$ are defined in the regions $\Omega^{(k)}$ and $\Omega^{(l)}$, which we have identified as intracellular and extracellular regions in the above. The membrane acts primarily as a capacitor, but possesses ionic channels through which transmembrane current can flow.

Boltzmann constant and $T$ the absolute temperature. The fixed background charge density (if any) is given by $\rho_0$.

The electrostatic potential $\phi$ is determined implicitly by the electroneutrality condition (3). We can obtain an equation that is satisfied by $\phi$ by taking the derivative of (3) with respect to time $t$:

$$\sum_{i=1}^{N} qz_i \frac{\partial c_i}{\partial t} = \sum_{i=1}^{N} qz_i \nabla \cdot \boldsymbol{f}_i = \nabla \cdot (a \nabla \phi + \nabla b) = 0, \tag{4}$$

where

$$a(\boldsymbol{x}, t) = \sum_{i=1}^{N} \frac{(qz_i)^2 D_i}{k_B T} c_i(\boldsymbol{x}, t), \quad b(\boldsymbol{x}, t) = \sum_{i=1}^{N} qz_i D_i c_i(\boldsymbol{x}, t). \tag{5}$$

Thus, $\phi$ satisfies an elliptic constraint such that electroneutrality is satisfied at each instant of time.

We now turn to the boundary conditions, satisfied at both the intracellular and extracellular sides of the cell membrane. Biological membranes consist largely of a lipid bilayer. In this cell membrane are embedded ionic channels and transporters through which certain ionic species may pass.

Across the cell membrane, a jump in electrostatic potential (*membrane potential*) is maintained, and the cell membrane acts as a capacitor. There is, therefore, a thin layer (*space charge layer*) on both sides of the membrane where electric charge accumulates. The thickness of this layer is on the order of the *Debye length* which measures approximately 1 nm in physiological systems. In (3), we have taken the

electroneutrality condition to hold inside and outside the cell, and this implies that we must treat the effect of having Debye layers in the form of boundary conditions.

The strength of the ionic current through an open ionic channel is determined by the membrane potential and ionic concentrations on either side of the membrane. Ionic channels may open or close, and the dynamics of this *gating* is also determined in large part by the membrane potential and ionic concentrations [10].

The boundary conditions satisfied on the $\Omega^{(k)}$ face of the membrane $\Gamma^{(kl)}$ are

$$\frac{\partial \sigma_i^{(k)}}{\partial t}(\boldsymbol{x}_m, t) + j_i^{(kl)}(\boldsymbol{x}_m, t) = q z_i \boldsymbol{f}_i^{(k)} \cdot \boldsymbol{n}^{(kl)}(\boldsymbol{x}_m). \tag{6}$$

All variables are defined on the boundary, and a spatial location on the boundary is denoted by $\boldsymbol{x}_m$. The term $j_i^{(kl)}$ denotes the transmembrane current per unit area from region $\Omega^{(k)}$ into $\Omega^{(l)}$. We note by definition that $j_i^{(kl)} = -j_i^{(lk)}$. The variable $\sigma_i^{(k)}$ denotes the contribution of the $i$-th species of ion to surface charge per unit area. The above boundary condition states that the current that flows onto the membrane either goes across the membrane through ionic channels, or contributes to change in surface charge.

In order to make (6) into a useful boundary condition, we must be able to write $j_i^{(kl)}$ and $\sigma_i^{(k)}$ in terms of $c_i$ and $\phi$. The surface charge density $\sigma_i^{(k)}$ is expressed as

$$\sigma_i^{(k)} = \lambda_i^{(k)}(\boldsymbol{x}_m, t)\sigma^{(k)}(\boldsymbol{x}_m, t), \qquad \sigma^{(k)} = C_{\mathrm{m}}\phi^{(kl)}, \tag{7}$$

$$\frac{\partial \lambda_i^{(k)}}{\partial t} = \frac{\tilde{\lambda}_i^{(k)} - \lambda_i^{(k)}}{\tau}, \qquad \tilde{\lambda}_i^{(k)}(\boldsymbol{x}_m, t) = \frac{z_i^2 c_i^{(k)}}{\sum_{i'=1}^{N} z_{i'}^2 c_{i'}^{(k)}}. \tag{8}$$

Here, $c_i^{(k)}$ and $\phi^{(k)}$ denote limiting values of $c_i$ and $\phi$ as one approaches the membrane from the $\Omega^{(k)}$ side of the membrane $\Gamma^{(kl)}$ and $\phi^{(kl)} = \phi^{(k)} - \phi^{(l)}$ is the membrane potential. $\tau$ is a relaxation time constant which we shall discuss shortly. $\sigma^{(k)}$ is the total charge on the $\Omega^{(k)}$ side of the membrane surface and is the product of $C_{\mathrm{m}}$, the capacitance of the membrane and the membrane potential $\phi^{(kl)}$. Since $\phi^{(kl)} = -\phi^{(lk)}$, (7) implies that $\sigma^{(k)} = -\sigma^{(l)}$ at each point of the membrane. Thus, like a capacitor, each patch of membrane is electrically neutral, since the charge stored on one side of the membrane balances the charge stored on the other side.

Note that $\lambda_i^{(k)}$ is the fractional contribution of the $i$-th species of ion to the surface charge density on face $k$ of the membrane (7). The quantity $\lambda_i^{(k)}$ relaxes to $\tilde{\lambda}_i^{(k)}$ with time constant $\tau = r_d^2/D_0 = 1$ ns, the diffusive time scale within the Debye layer ($r_d$ is the aforementioned Debye length and $D_0$ is a representative diffusive constant for ions). This relaxation time is introduced to avoid an instability that occurs if we formally take the limit $\tau \to 0$ and set $\lambda_i^{(k)} = \tilde{\lambda}_i^{(k)}$; see the Appendix for further discussion and [25; 24] for details. The choice $\tau = 1$ ns is large enough to avoid

this instability and yet small enough that $\lambda_i^{(k)}$ remains close to $\tilde{\lambda}_i^{(k)}$ at all times in any practical application.

The derivation of specific formula for $\tilde{\lambda}_i^{(k)}$ given in (8) requires a closer look at the ionic composition of the space charge layer. A derivation by physical reasoning in [27] and by matched asymptotic analysis in [25] and [24]. A quick derivation is given in the Appendix for convenience of the reader. The expression for $\tilde{\lambda}_i^{(k)}$ states that the fractional contribution of each species ion to the surface charge on one face of the membrane is given by the concentration of that ion species in the bulk solution near that face of the membrane weighted by the *square* of the charge carried by that species of ion. This result is closely related to the concept of *ionic strength* in electrochemistry [5], which is defined as $\frac{1}{2}z_i^2 c_i$. Note the implication that ions of either sign can contribute, for example, to a positive space charge layer. Such a layer involves an increased concentration of positive ions and a reduced concentration of negative ions in comparison to the concentrations of these ions in the electroneutral bulk solution outside of the space charge layer.

The interpretation of $\lambda_i^{(k)}$ as the fractional contribution of the $i$-th ion species to the surface charge on face $k$ of the membrane requires that $\sum_i \lambda_i^{(k)} = 1$ be satisfied identically, at all membrane locations for all time. To verify this condition, sum both parts of (8) from $i = 1, \ldots, N$. The second part gives $\sum_i \tilde{\lambda}_i^{(k)} = 1$, and the first part therefore shows that $\sum_i \lambda_i^{(k)}$ relaxes to 1, and indeed is identically equal to 1 if it is equal to 1 initially. We assume in the sequel that the initial values of $\lambda_i^k$ have this property.

We now discuss $j_i$, the transmembrane currents. Biophysically, these are currents that flow through ion channels, transporters, or pumps that are located within the cell membrane [1; 10; 15]. We use the formalism of Hodgkin and Huxley for ion channel currents [11; 16; 18], generalized to allow for nonlinear instantaneous current-voltage relations and ion concentration effects.

$$j_i^{(kl)}(\boldsymbol{x}_m, t) = J_i^{(kl)}(\boldsymbol{x}_m, s^{(kl)}, \phi^{(kl)}, c^{(k)}, c^{(l)}). \tag{9}$$

The transmembrane current density $J_i^{(kl)}$ is a function characteristic of the channels (possibly of more than one type) that carry the $i$-th species of ion across the membrane separating $\Omega^{(k)}$ from $\Omega^{(l)}$. The explicit dependence of $J_i^{(kl)}$ on $\boldsymbol{x}$ reflects the possible inhomogeneity of the membrane: the density of channels may vary from one location to another. The other arguments of $J_i^{(kl)}$ are as follows.

First, there is a vector of gating variables $s^{(kl)}(\boldsymbol{x}_m, t) = (s_1^{(kl)}, \ldots, s_G^{(kl)})$ where $G$ is the total number of gating variables in all of the channel types that arise in our system. (Only some of these influence the channels that conduct ions of species $i$.) The individual components $s_g^{(kl)}$ of $s^{(kl)}$ are dimensionless variables as introduced by Hodgkin and Huxley [11] that take values in the interval [0, 1] and satisfy ordinary

differential equations of the form,

$$\frac{\partial s_g^{(kl)}}{\partial t} = \alpha_g^{(kl)}(\phi^{(kl)})(1 - s_g^{(kl)}) - \beta_g^{(kl)}(\phi^{(kl)})s_g^{(kl)} \tag{10}$$

for $g = 1, \ldots, G$ where $\alpha_g^{(kl)}$ and $\beta_g^{(kl)}$ are positive, empirically defined functions of the transmembrane potential. In general, the gating variables obey a more complicated ordinary differential equation:

$$\frac{\partial s_g^{(kl)}}{\partial t} = f_g^{(kl)}(s^{(kl)}, \phi^{(kl)}, c^{(k)}, c^{(l)}). \tag{11}$$

We note the conditions $j_i^{(kl)} = -j_i^{(lk)}$ and $\phi^{(kl)} = -\phi^{(lk)}$ impose the following constraints on the form of the functions $\alpha_g^{(kl)}$, $\beta_g^{(kl)}$ and $f_g^{(kl)}$:

$$\alpha_g^{(kl)}(\phi^{(kl)}) = \alpha_g^{(lk)}(\phi^{(lk)}), \quad \beta_g^{(kl)}(\phi^{(kl)}) = \beta_g^{(lk)}(\phi^{(lk)}), \tag{12}$$

$$f_g^{(kl)}(s^{(kl)}, \phi^{(kl)}, c^{(k)}, c^{(l)}) = f_g^{(lk)}(s^{(lk)}, \phi^{(lk)}, c^{(l)}, c^{(k)}). \tag{13}$$

The next argument of $J_i^{(kl)}$ is again the transmembrane potential $\phi^{(kl)}$. Holding the other arguments fixed in $J_i^{(kl)}$, and letting only $\phi^{(kl)}$ vary, we get the instantaneous current-voltage relationship for current carried by the $i$-th ion from $\Omega^{(k)}$ to $\Omega^{(l)}$ at point $\boldsymbol{x}$ at time $t$.

The last two arguments of $J_i^{(kl)}$ are the vectors of ion concentrations on the two sides of the membrane: $c^{(k)} = (c_1^{(k)}, \ldots, c_N^{(k)})$ and similarly for $c^{(l)}$. By including the whole vector of ion concentrations, we allow for the possibility that the current carried by the $i$-th species of ion is influenced by the concentrations of other ionic species on the two sides of the membrane. This, for example, is the case with calcium gated potassium channels ($K_{Ca}$ channels) whose potassium conductance is controlled by the intracellular calcium concentration [10].

Equations (1)–(3) with the boundary condition (6) is the model we consider in this paper. We shall call this model the *electroneutral model*.

## 3. Cable model and multiple timescales

The above electroneutral model provides a more detailed description of cellular electrophysiology than the more familiar one-dimensional cable model (see (20), below). In this section, we sketch the derivation of the cable model from the electroneutral model. We do so in part to confirm that the electroneutral model contains the cable model as a limiting case, but also to bring out the different time scales that will complicate the numerical solution of the equations of the electroneutral model. For a more complete exposition of the derivation sketched here, see [25].

First, recall from (4) that $\phi$ satisfies an elliptic equation. The boundary conditions for this equation can be obtained by the sum over $i$ in (6):

$$C_{\mathrm{m}}\frac{\partial \phi^{(kl)}}{\partial t} + I^{(kl)}(\boldsymbol{x}_m, t) = -(a\nabla\phi + \nabla b)\cdot \boldsymbol{n}, \tag{14}$$

where we have used $\sum_{i=1}^{N}\sigma_i = C_{\mathrm{m}}\phi^{(kl)}$ (7) and $I^{(kl)} \equiv \sum_{i=1}^{N} j_i^{(kl)}$. The coefficients $a$ and $b$ were given in (5). Thus, the electrostatic potential satisfies an elliptic problem with an evolutionary boundary condition satisfied at the membrane.

Suppose now that the ionic concentrations inside and outside the cell do not change appreciably in the time of biophysical interest, and that the ionic concentrations gradients are negligible. Then, we have only to track the evolution of the electrostatic potential and the coefficient $a$ and $b$ of (4) is constant within each of the domains separated by the membrane. Thus, (4) and (14) can now be written as

$$\Delta\phi = 0 \qquad \text{in } \Omega^{(k)}, \Omega^{(l)}, \tag{15}$$

$$C_{\mathrm{m}}\frac{\partial \phi^{(kl)}}{\partial t} + I^{(kl)} = -a^{(k)}\frac{\partial \phi}{\partial \boldsymbol{n}^{(kl)}} = -a^{(l)}\frac{\partial \phi}{\partial \boldsymbol{n}^{(kl)}} \qquad \text{on } \Gamma^{(kl)}. \tag{16}$$

where $a^{(k)}$ and $a^{(l)}$ are now constants defined within each domain. The gradient of $b$ disappears from the equations because we have assumed that we do not have a concentration gradient. We see that the evolution of the electrostatic potential is completely specified by what happens at the boundary. We note that Equations (15) and (16) have been used to model cellular electrophysiology and is also the basis for the bidomain model used in tissue level electrophysiology [8; 3; 28; 16].

Consider a simple situation in which we have just two regions, one intracellular and the other extracellular. We take the intracellular region to be a bounded simply connected set whereas the extracellular space its complement in $\mathbb{R}^3$. For simplicity, suppose that $a^{\mathrm{int}} = a^{\mathrm{ext}}$. Consider the following boundary value problem for $\phi$.

$$\Delta\phi = 0 \qquad \text{in } \Omega^{\mathrm{ext}}, \Omega^{\mathrm{int}}, \tag{17}$$

$$\phi_{\mathrm{m}} \equiv \phi^{\mathrm{int}} - \phi^{\mathrm{ext}} = f, \quad \frac{\partial \phi^{\mathrm{int}}}{\partial \boldsymbol{n}} = \frac{\partial \phi^{\mathrm{ext}}}{\partial \boldsymbol{n}} \qquad \text{on } \Gamma. \tag{18}$$

where $f$ is some function given on the membrane $\Gamma$ and $\boldsymbol{n}$ is the unit normal pointing from the intracellular to extracellular side of the cell. We require that $\phi$ decays to 0 at infinity. The above boundary value problem defines a map from $\phi_{\mathrm{m}} = f$ to $\partial\phi^{\mathrm{int}}/\partial\boldsymbol{n} = \partial\phi^{\mathrm{ext}}/\partial\boldsymbol{n}$. This is similar to the usual Dirichlet-to-Neumann map on a single domain, except that we are here solving a Laplace problem on both sides of the membrane interface, and the input we are given is the *jump* in the electrostatic potential. We denote this map as $\mathscr{L}$. Using this map, and the simplification $a = a^{\mathrm{int}} = a^{\mathrm{ext}}$, we can write (15) and (16) as

$$C_{\mathrm{m}}\frac{\partial \phi_{\mathrm{m}}}{\partial t} + I = -a\mathcal{L}\phi_{\mathrm{m}}. \tag{19}$$

We now clearly see that the evolution of $\phi$ is confined to the boundary. It is straightforward to show that $\mathcal{L}$ can be extended to a nonnegative self-adjoint operator on square integrable functions on $\Gamma$. This tells us that $\phi_{\mathrm{m}}$ evolves according to an evolutionary equation similar to a reaction-diffusion equation, where the Laplacian is replaced with $-1$ times $\mathcal{L}$. Thus, there is a "diffusive" process that takes place on the two dimensional membrane surface. We shall call this *membrane potential diffusion*.

We would like to compare the speeds of the two dissipative processes at play: ionic diffusion and membrane potential diffusion. The "diffusion" coefficient $a/C_{\mathrm{m}}$ in front of the operator $-\mathcal{L}$ in (19) has dimensions of length/time. Therefore, it cannot be compared directly with the ionic diffusion coefficient $D_i$ which has dimensions length$^2$/time. However, if there is a natural characteristic length scale $L$ associated with the geometry of the system, the combination $D_\phi \equiv aL/C_{\mathrm{m}}$ may be used as a value to be compared with $D_i$.

Suppose the cell is cylindrical in shape. Assuming that the membrane potential varies slowly on the length scale defined by the radius of the cylinder, (19) can be further reduced to the following one-dimensional reaction diffusion equation.

$$C_{\mathrm{m}}\frac{\partial \phi_{\mathrm{m}}}{\partial t} + I = \frac{aR}{2}\frac{\partial^2 \phi_{\mathrm{m}}}{\partial z^2}, \tag{20}$$

where $R$ is the radius of the cylinder and $z$ is the axial coordinate. This is nothing other than the cable model. A quick derivation of this is given in the Appendix. The factor $R/2$ comes from the ratio of the cylindrical cross-sectional area to the circumference: $\pi R^2/(2\pi R)$. In (20), $L = R/2$ emerges as the natural characteristic length scale, and $D_\phi = aR/(2C_{\mathrm{m}})$. Let us examine the ratio between $D_\phi$ and $D_i$.

$$D_\phi = \frac{aR}{2C_{\mathrm{m}}} = \sum_{i=1}^{N} \frac{L(qz_i)^2 c_i}{C_{\mathrm{m}} k_B T} D_i = \sum_{i=1}^{N} \frac{Lqc_i}{C_{\mathrm{m}}(k_B T/q)} \frac{1}{2} z_i^2 D_i, \tag{21}$$

where we used (5) in the second equality. Given that $z_i^2$ is an order 1 quantity,

$$\frac{D_\phi}{D_i} \approx \frac{Lqc_0}{C_{\mathrm{m}}(k_B T/q)} = 10^4 \sim 10^6, \tag{22}$$

where $c_0$ is the typical ionic concentration. The above is a ratio of the absolute amount of charge in the electrolyte solution to the membrane surface charge, which turns out to be $10^4$ to $10^6$ in physiological systems. This illustrates the presence of two disparate time scales in the problem.

That membrane potential diffusion is fast and dissipative has important implications for time stepping, to be discussed in Section 5.

## 4. Spatial discretization

**4.1.** ***Finite volume method.*** We shall use a finite volume discretization in space [21]. Take any finite volume $\Omega_{\text{fv}}$ contained in $\Omega^{(k)}$ and suppose the boundary of this region is comprised of two components, the $\Gamma_{\text{el}}$ component that faces the electrolyte solution, and the $\Gamma_{\text{m}}$ component that faces the membrane. It may be the case that either $\Gamma_{\text{el}}$ or $\Gamma_{\text{m}}$ is empty. For each ionic species, we have the following conservation relation in integral form:

$$\begin{aligned}\int_{\Omega_{\text{fv}}} \frac{\partial c_i}{\partial t} dV &= \int_{\Gamma_{\text{el}} \cup \Gamma_{\text{m}}} \boldsymbol{f}_i \cdot \boldsymbol{n} dA \\ &= -\int_{\Gamma_{\text{el}}} D_i \big(\nabla c_i + \frac{q z_i c_i}{k_B T} \nabla \phi\big) \cdot \boldsymbol{n} dA \\ &\qquad + \int_{\Gamma_{\text{m}}} \frac{1}{q z_i} \big(C_{\text{m}} \frac{\partial (\lambda_i^{(k)} \phi^{(kl)})}{\partial t} + j_i^{(kl)}\big) dA. \quad (23)\end{aligned}$$

The electroneutrality condition is equivalent to saying that

$$\rho_0 + \sum_{i=1}^{N} q z_i c_i = 0 \text{ at } t = 0, \quad \sum_{i=1}^{N} q z_i \frac{\partial c_i}{\partial t} = 0, \quad \text{for } t > 0. \quad (24)$$

As long as the electroneutrality condition is satisfied at $t = 0$, we have only to consider the time derivative of the electroneutrality condition for time $t > 0$. Therefore, we can obtain the electroneutrality condition expressed in integral form by taking (23), multiplying by $q z_i$ and summing in $i$.

$$\begin{aligned}0 = &-\int_{\Gamma_{\text{el}}} \Big( \sum_{i=1}^{N} q z_i D_i \Big(\nabla c_i + \frac{q z_i c_i}{k_B T} \nabla \phi\Big) \cdot \boldsymbol{n} \Big) dA \\ &+ \int_{\Gamma_{\text{m}}} \Big( C_{\text{m}} \frac{\partial \phi^{(kl)}}{\partial t} + \sum_{i=1}^{N} j_i^{(kl)} \Big) dA. \quad (25)\end{aligned}$$

Note that (23) and (25) are equivalent to the differential equations since the finite volume $\Omega_{\text{fv}}$ is arbitrary.

In the finite volume discretization, we partition the spatial region into a finite number of finite volumes (FVs), and apply (23) and (25) on each FV. We then approximate the volume and surface integrals that appear in the integral conservation relations.

For simplicity, consider a two-dimensional situation. Discretize space into polygonal finite volumes. For each FV we designate a representative location $\boldsymbol{x}_c$ where we define the value of the physical variables. Equation (1) for ion conservation

can be discretized using a finite volume approach in the following fashion.

$$\left.\frac{\partial c_i}{\partial t}\right|_{\boldsymbol{x}=\boldsymbol{x}_c} \approx \frac{1}{V}\int_{\text{finite volume}} \frac{\partial c_i}{\partial t}\, dV = -\frac{1}{V}\int_{\text{faces of FV}} \boldsymbol{f}\cdot\boldsymbol{n}\, dA$$
$$\approx -\frac{1}{V}\sum_q e_q F^q, \tag{26}$$

where $V$ is the volume (in two dimensions the area) of the FV, $\ell$ labels the faces (polygonal sides), and $e_\ell$ is the area (in two dimensions the length) of the face $\ell$. $F^\ell$ is an approximation to the true flux $\boldsymbol{f}\cdot\boldsymbol{n}$ evaluated on face $\ell$. The discrete evolution equation is thus

$$\frac{\partial c_i}{\partial t} = -\frac{1}{V}\sum_\ell e_\ell F^\ell. \tag{27}$$

Label the FVs by $p$ and write the flux density approximation from FV $p$ to $p'$ as $F^{(p,p')}$. As long as $F^{(p,p')} = -F^{(p',p)}$, we have discrete conservation of $c_i$. Thus, it is straightforward with the finite volume method construct a conservative numerical scheme. In our case, however, there is the unusual complication that we have to account not only for ions in the interiors of the FVs but also for the ions in the space charge layers. Because of this, it will not always be the case that $F^{(p,p')} = -F^{(p',p)}$, but our scheme will be conservative anyway, as explained below.

As we shall see, the discretization of the electroneutrality condition will be obtained by multiplying (27) by $qz_i$ and summing in $i$. This can be seen as a discretization of the integral charge conservation relation (25).

**4.2.** ***Cylindrical geometry.*** We have developed finite volume schemes adapted to two types of simulations, one for arbitrary two-dimensional membrane geometry, and the other for cylindrical geometry. We first discuss the finite volume discretization for cylindrical geometry.

Take a cylindrical coordinate system with the axial coordinate $z$ and the radial coordinate $r$. We seek solutions that are axisymmetric. We discretize in $r$ and $z$. We have a series of FVs whose shape is a torus with a rectangular cross-section. Each FV will generically have four faces at which it touches other FVs. FVs are indexed by $p$ and the associated quantities of the FV $p$ are labeled with the subscript or superscript $p$. Consider an FV $p$. Let the width of this FV in the $r$ direction be $h_p^r$ and that in the $z$ direction be $h_p^z$. We let $h_p^r < Kh$ and $h_p^z < Kh$ for some constant $K$ uniformly for all $p$ and take $h \to 0$. To each FV we apply the divergence theorem and its approximation, as we did in (26) and (27).

For cylindrical geometry, we require that the membrane conform to the FV boundaries. That is to say, the membrane patches can be described by $z = \text{const}$ or $r = \text{const}$. FV faces that coincide with the membrane will be referred to as

*membrane faces*. Non-membrane faces will be referred to as *ordinary faces*. To each ordered pair of FVs $p$ and $p'$ we associate two quantities $e^{(p,p')}$ and $\gamma^{(p,p')}$. If FVs $p$ and $p'$ are adjacent to each other through an ordinary face, we let $e^{(p,p')}$ be the area of this membrane face. Otherwise we set $e^{(p,p')} = 0$. Likewise, if FVs $p$ and $p'$ are adjacent through a membrane face, we set $\gamma^{(p,p')}$ to be its area and 0 otherwise. By definition, $e^{(p,p')} = e^{(p',p)}$ and likewise for $\gamma^{(p,p')}$. If $e^{(p,p')} \neq 0$ or $\gamma^{(p,p')} \neq 0$, we let $F^{(p,p')}$ and $G^{(p,p')}$ denote the flux density from FV $p$ to FV $p'$ respectively. Otherwise, we set $F^{(p,p')} = 0$ or $G^{(p,p')} = 0$. The specific forms of $F^{(p,p')}$ and $G^{(p,p')}$ will be discussed shortly. If $\gamma^{(p,p')} \neq 0$ , we must define membrane associated quantities that correspond to this ordered pair. They include the gating variables $s_g^{(p,p')}$ and the membrane charge fraction $\lambda_i^{(p,p')}$. The former satisfy $s_g^{(p,p')} = s_g^{(p',p)}$ and their associated evolution equations satisfy symmetry conditions that correspond to (12) and (13). We let $\lambda_i^{(p,p')}$ denote the membrane charge fraction of the membrane patch $(p, p')$ found on the membrane surface facing FV $p$. There is no symmetry relation between $\lambda_i^{(p,p')}$ and $\lambda_i^{(p',p)}$ since they are different physical entities. FVs with one or more membrane faces will be called *membrane FVs*, whereas FVs without membrane faces will be called *ordinary FVs*.

Consider FV $p$ whose coordinates are given by $z_{p0} < z < z_{p1}$ and $r_{p0} < r < r_{p1}$. The discrete evolution equation for ionic concentrations $c_i^p$ in FV $p$ are

$$\frac{\partial c_i^p}{\partial t} = -\frac{1}{V_p} \sum_{p' \neq p} (e^{(p,p')} F_i^{(p,p')} + \gamma^{(p,p')} G_i^{(p,p')}), \tag{28}$$

where $V_p$ is the volume of the FV $p$. We think of $c_i^p$ and $\phi^p$, the physical variables associated with the FV $p$, as being defined at the center of the axial cross-section of FV $p$. That is to say, the representative point $\boldsymbol{x}_c$ in (26) is taken to be at $r = (r_{p0} + r_{p1})/2$, and $z = (z_{p0} + z_{p1})/2$. For an ordinary FV, the second sum in (28) is 0.

All we need now in (28) are the approximate flux density expressions $F_i^{(p,p')}$ and $G_i^{(p,p')}$. For discretization of the flux density in the axial direction, we take

$$F_i^{(p,p')} = D_i \left( \frac{c_i^p - c_i^{p'}}{(h_{p'}^z + h_p^z)/2} + \frac{q z_i}{k_B T} \frac{h_{p'}^z c_i^p + h_p^z c_i^{p'}}{h_{p'}^z + h_p^z} \frac{\phi^p - \phi^{p'}}{(h_{p'}^z + h_p^z)/2} \right). \tag{29}$$

Note that this expression changes sign if $p$ and $p'$ are exchanged, making this a conservative discretization. We take care in constructing our mesh that the mesh width in the $z$ direction changes smoothly as a function of the $z$ coordinate of the representative point of the FV. For fluxes in the radial direction, we discretize in exactly the same fashion.

We now turn to the approximation to the membrane fluxes $G_i^{(p,p')}$.

$$qz_i G_i^{(p,p')} = C_{\mathrm{m}} \frac{\partial(\lambda_i^{(p,p')} \phi_{\mathrm{m}}^{(p,p')})}{\partial t} + j_i^{(p,p')}(s^m, \phi_{\mathrm{m}}^{(p,p')}, c^p, c^{p'}), \tag{30}$$

$$\phi_{\mathrm{m}}^{(\mathrm{p,p'})} = \phi^p - \phi^{p'}. \tag{31}$$

We evaluate the membrane quantities $c$ (vector of ionic concentrations $(c_1, \ldots, c_N)$) and $\phi_{\mathrm{m}}$ using values at the representative points $\boldsymbol{x}_c$ of FVs $p$ and $p'$. The function $j_i^{(p,p')}$ satisfies symmetry conditions equivalent to (13) so that $j_i^{(p,p')} = -j_i^{(p',p)}$. Note that in general $G_i^{(p,p')} \neq -G_i^{(p',p)}$, because of the presence of the surface charge

$$\sigma_i^{(p,p')} \equiv \lambda_i^{(p,p')} C_{\mathrm{m}} \phi_{\mathrm{m}}^{(p,p')}.$$

Our discretization is conservative nevertheless in the following sense. The quantity

$$V_p c_i^p + \frac{1}{qz_i} \sum_{p' \neq p} \gamma^{(p,p')} \sigma_i^{(p,p')} \tag{32}$$

will be conserved thanks to the symmetry conditions satisfied by $F_i^{(p,p')}$ and $j_i^{(p,p')}$. Expression (32) is the total ionic content in the FV $p$, taking into account the amount of ion that resides within the space charge layer.

We finally note that the discretization of the electroneutrality condition for each FV can be obtained by multiplying the discrete evolution equation (28) by $qz_i$ and summing them over $i$ (under the assumption that the initial configuration satisfies the electroneutrality condition):

$$0 = \sum_{i=1}^{N} qz_i \sum_{p' \neq p} (e^{(p,p')} F_i^{(p,p')} + \gamma^{(p,p')} G_i^{(p,p')}). \tag{33}$$

This is precisely the discretization of (25).

By expanding these flux approximations in Taylor series and substituting into (26), one can easily obtain the local truncation error for each FV. The local truncation error for ordinary FVs is $\mathbb{O}(h)$ and is $\mathbb{O}(1)$ for membrane FVs. We shall nonetheless observe approximate second order convergence in space in the cylindrical geometry case, as we shall see in Section 7.

As for boundary conditions at the outer rim of the computational domain, we shall make use a no-flux boundary condition.

**4.3.** ***Arbitrary two-dimensional membrane geometry.*** We have developed code that handles two-dimensional arbitrary membrane geometry. The ideas are the same as for the cylindrical case. We shall use an *embedded boundary method*, where a uniform Cartesian grid is used over most of the computational domain, except where the grid is cut by the membrane [13; 7; 23].

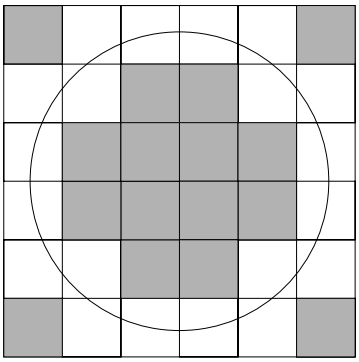

**Figure 2.** Grid for two-dimensional simulation. The shaded FVs are the ordinary FVs whereas the nonshaded FVs are the membrane FVs. To each membrane patch, there are two membrane FVs. In the above figure, there are 36 meshes, 16 ordinary FVs, and 40 membrane FVs.

Henceforth, we shall use the word *mesh* to denote the uniform Cartesian grid laid on the computational domain, and also to denote the square patches that result from this grid (Figure 2). We shall take the mesh sides to have length $h$. An FV is the same thing as a mesh if the membrane does not cut through this mesh. If the membrane does cut through the mesh, we approximate this membrane cut by a straight line, and the resulting two polygons will be our FVs that correspond to this mesh. We shall call an uncut Cartesian mesh an *ordinary* FV. An FV that is cut out of a Cartesian mesh by the membrane will be called a *membrane* FV. We shall label our FVs and their associated quantities with subscript or superscript $p$.

When a membrane cuts through a mesh, two FVs will be generated. These two FVs share a common membrane patch. These are the *membrane faces*, whereas other faces of the FV are the *ordinary faces*. Each face is flanked by two FVs $p$ and $p'$, and the faces are labeled by the ordered pair $(p, p')$. As in the cylindrical case, we associate with each membrane patch $(p, p')$ its attendant physical quantities.

In the case of an ordinary FV, we shall take the representative point $\boldsymbol{x}_c$, with which the values of the physical variables are associated, to be the center of the FV. For a membrane FV, we shall take $\boldsymbol{x}_c$ to be the center of the Cartesian mesh from which the FV was cut. Thus, there will be cases in which $\boldsymbol{x}_c$ geometrically lies outside the FV. Conceptually, this involves the smooth extrapolation of a function defined on one side of the membrane to the other side of the membrane. For each membrane FV, there is another membrane FV that shares the same membrane patch which was therefore cut out of the same mesh. These two membrane FVs have representative points $\boldsymbol{x}_c$ that coincide geometrically but are computationally distinguished.

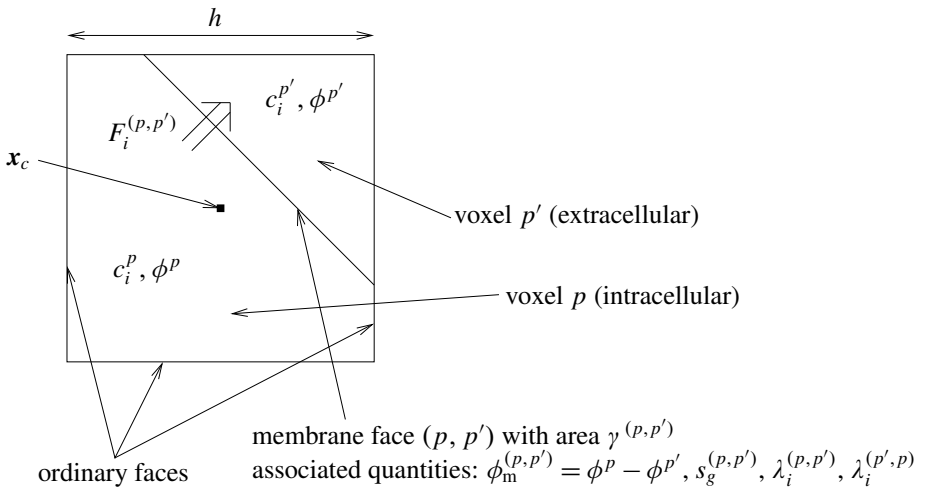


**Figure 3.** A membrane FV and its associated quantities.

The structure of the discretization exactly parallels that for the cylindrical case. The evolution equation for the concentration discretized in space will be the same as (28). We now briefly discuss approximation of the flux terms $F_i^{(p,p')}$ and $G_i^{(p,p')}$. For $F_i^{(p,p')}$, regardless of whether $e^{(p,p')} = h$ or otherwise, we shall use

$$F_i^{(p,p')} = D_i\Big(\frac{c_i^p - c_i^{p'}}{h} + \frac{qz_i(c_i^p + c_i^{p'})}{2k_BT}\frac{\phi^p - \phi^{p'}}{h}\Big). \tag{34}$$

For the membrane flux, we use the same expression as (30).

As in the cylindrical case, one can determine the local truncation error of the above scheme. For ordinary FVs, the truncation error is $\mathbb{O}(h^2)$ whereas for membrane FVs, the error is $\mathbb{O}(1)$. Nonetheless, we shall see in Section 8 that we generally observe obtain linear to supralinear convergence in space.

To handle arbitrary membrane geometry, we must generate the necessary geometry data at the membrane where the mesh is cut. We have written a custom mesh generator to perform this task. It takes the characteristic function of a region as input to generate the necessary data. The mesh generator approximates a cut by the membrane as a straight line, and cannot handle nongeneric cases of degenerate geometry. When the volume of a membrane FV is less than $10^{-5}$ times the volume of an ordinary mesh, this FV is ignored.

## 5. Temporal discretization

For our algorithm overall, we adopt an operator splitting approach. We split each time evolution step into the *gating substep* in which we update the gating variables $s_g$ defined on the membrane followed by the *potential/concentration substep* in

which we update the electrostatic potential and ionic concentrations. This splitting allows us to significantly reduce computational cost and makes the code modular by making it easy to supply the PDE system with different gating variable kinetics, which varies widely depending on the biophysical system of interest. Since the splitting error is first order, the time-stepping error should be first order overall so long as we use a first order method for the gating part and the potential/concentration part of the time stepping.

In the gating substep, we treat the gating variables implicitly while we treat the electrostatic potential and concentrations implicitly. In the potential/concentration substep, we treat the electrostatic potential and concentrations implicitly while treating the gating variables explicitly. We now discuss this latter substep in greater detail.

Recall from the discussion of Section 3 that the system of equations has two diffusive time scales. For parameter ranges of biophysical interest, the dissipative nature of membrane potential "diffusion" in particular makes it prohibitively expensive to use an explicit time-stepping scheme, rather than the ionic diffusion, as we shall see below. We saw in Section 3 that the evolution of the electrostatic potential is governed by (19) under the approximation of constant concentration:

$$\frac{\partial \phi_{\mathrm{m}}}{\partial t} + \frac{I(\phi_{\mathrm{m}})}{C_{\mathrm{m}}} = -\frac{a}{C_{\mathrm{m}}} \mathcal{L} \phi_{\mathrm{m}}, \tag{35}$$

where we have explicitly noted the dependence of $I$ on $\phi_{\mathrm{m}}$. The behavior of $\mathcal{L}$ can be gleaned by looking at how $\mathcal{L}$ acts in the special case when $\Omega^{\mathrm{int}}$ and $\Omega^{\mathrm{ext}}$ are the upper and lower half spaces of $\mathbb{R}^3$ respectively. By employing Fourier analysis, we can see that the component with wave number $\boldsymbol{k}$ on the membrane is multiplied in amplitude by a factor proportional to $|\boldsymbol{k}|$. This can also be inferred by looking at the "diffusion" coefficient $a/C_{\mathrm{m}}$, which has dimensions length/time. Note that this is different from the diffusion operator where the amplitude is multiplied by $|\boldsymbol{k}|^2$. This implies that as the mesh width on the membrane is made smaller, one should refine the time step proportionally to the mesh width if we are to use an explicit scheme.

For physiologically relevant systems, the "diffusion" constant in (35), $a/C_{\mathrm{m}}$, is approximately equal to $10^5\ \mu$m/ms. We may thus infer that a mesh width on the order of $1\ \mu$m will necessitate a time step on the order of 10 ns if an explicit scheme is used. On the other hand, $D_i$ is on the order of $1\ \mu\mathrm{m}^2/\mathrm{ms}$. Thus, the time step restriction imposed by ionic diffusion is much less stringent, on the order of submilliseconds. The time step restriction thus arises chiefly from membrane potential diffusion, and a time step on the order of nanoseconds is unacceptable given that biophysical phenomena of interest occur on the millisecond time scale [1; 18; 10]. For example, a single synaptic transmission event in the central nervous

system, a process we believe our modeling methodology to be useful for, typically has a duration on the order of 1–10 ms [18; 15].

We note that in [29], the authors introduce a one-dimensional model of cellular electrophysiology incorporating ionic diffusion, where they use time steps as small as 1 ns to simulate their system. This small time step requirement is related to the time step restriction that would apply to an explicit scheme in our case, too, as discussed above. In [18], the author argues that this has been a major impediment in incorporating electrodiffusion of ions in modeling studies of cellular or subcellular electrophysiology.

This difficulty is overcome by treating $\phi$ and $c_i$ implicitly in the potential/concentration step. The membrane potential $\phi_{\mathrm{m}}$ becomes an unknown to be determined. Note that $\phi_{\mathrm{m}}$ is the jump in $\phi$ across the cell membrane. We here have an elliptic interface problem in which we must solve for the unknown jumps across interfaces. In the context of time-dependent PDEs, similar problems arise in implicit discretizations of fluid structure interaction problems where one must solve for the unknown jump in the derivative of the velocity field across the immersed elastic interface. (see for example [22; 20]).

We label our time step by $n$, where $n$ is an integer. We let the time step duration be $\Delta t$. Suppose we know values of $s_g$, $c_i$, $\phi$ and $\lambda_i$ at time $(n-1)\Delta t$. In the gating substep, we advance $s_g$ to find values at time $n$ for every membrane patch.

$$\frac{s_g^{(p,p'),n} - s_g^{(p,p'),n-1}}{\Delta t} = f_g(s^{(p,p'),n}, \phi_{\mathrm{m}}^{(p,p'),n-1}, c^{p,n-1}, c^{p',n-1}). \tag{36}$$

Note that the evolution of the gating variables $s_g$ does not involve any spatial coupling, and thus, can be solved independently for every membrane patch.

In the potential/concentration substep, we advance $c_i$, $\phi$ and $\lambda_i$. Whether we are considering cylindrical geometry or arbitrary two-dimensional membrane geometry, the semidiscretized evolution equation for $c_i$ is (28). To discretize (28) in time, we use a backward Euler type discretization to march from time $(n-1)\Delta t$ to time $n\Delta t$, where $c_i$, $\phi$ and $\lambda_i$ are treated implicitly, whereas the gating variables $s_g$ are given quantities:

$$\frac{c_i^{p,n} - c_i^{p,n-1}}{\Delta t} = -\frac{1}{V_p} \sum_{p' \neq p} (e^{(p,p')} F_i^{(p,p'),n}(c_i^n, \phi^n) + \gamma^{(p,p')} G_i^{(p,p'),n}),$$

$$q z_i G_i^{(p,p'),n} = C_{\mathrm{m}} \Big( \frac{\lambda_i^{(p,p'),n} \phi_{\mathrm{m}}^{(p,p'),n} - \lambda_i^{(p,p'),n-1} \phi_{\mathrm{m}}^{(p,p'),n-1}}{\Delta t} \Big) + j_i^{(p,p'),n}(s^{(p,p'),n}, \phi_{\mathrm{m}}^{(p,p'),n}, c^{p,n-1}, c^{p',n-1}). \tag{37}$$

Note that $\phi$ is treated implicitly, so that the membrane potential $\phi_{\mathrm{m}}$ is an unknown

to be solved for at each time step. Of the arguments of $j_i^{(p,p'),n}$, we evaluate $c$ at time $(n-1)\Delta t$, whereas $\phi_{\mathrm{m}}$ and $s$ are evaluated at $n\Delta t$. The evolution of $\lambda_i$ is given by

$$\frac{\lambda_i^{(p,p'),n} - \lambda_i^{(p,p'),n-1}}{\Delta t} = \frac{\tilde{\lambda}_i^{(p,p'),n} - \lambda_i^{(p,p'),n}}{r_d^2/D_0}, \tag{38}$$

where $\tilde{\lambda}_i^{(p,p'),n}$ is evaluated using $c_i^{p,n}$. By summing (37) over $i$ and recalling that $\sum_i \tilde{\lambda}_i = 1$, we conclude that $\sum_i \lambda_i^{p,n}$ relaxes geometrically to 1 as $n$ increases. In particular, if this sum is equal to 1 initially it remains equal to 1 at every time step. Assuming that this is the case, we may multiply the above by $qz_i$ and sum in $i$ to get an equation in $\phi^{p,n}$.

$$-\frac{\rho_0^p + \sum_{i=1}^N qz_i c_i^{p,n-1}}{\Delta t} = -\frac{1}{V_p}\sum_{p'\neq p} e^{(p,p')} \sum_{i=1}^N qz_i F_i^{(p,p'),n}$$
$$-\frac{1}{V_p}\sum_{p'\neq p} \gamma^{(p,p')}\left(C_{\mathrm{m}}\left(\frac{\phi_{\mathrm{m}}^{(p,p'),n} - \phi_{\mathrm{m}}^{(p,p'),n-1}}{\Delta t}\right) + \sum_{i=1}^N j_i^{(p,p'),n}\right). \tag{39}$$

This can be viewed as the full discretization of (33). A subtle point is that we have only made use of the electroneutrality condition $\rho_0^p + \sum_i qz_i c_i^p = 0$ at time $n\Delta t$ and not at time $(n-1)\Delta t$; thus we retain the term $-(\rho_0^p + \sum_i qz_i c_i^{p,n-1})/\Delta t$ on the left hand side of (39). If electroneutrality were strictly satisfied at each time step, this term would be equal to 0. Since we cannot solve the above system of equations exactly in a numerical computation, electroneutrality is never strictly satisfied. The term $-\left(\rho_0^p + \sum_i qz_i c_i^{p,n-1}\right)/\Delta t$ acts to correct deviations from electroneutrality that may have been present at time $(n-1)\Delta t$.

## 6. Solution of nonlinear equations

We now solve the above discretized nonlinear algebraic equations for $c_i$, $\phi$ and $\lambda_i$. At each time step, we first solve for $\phi$ and $\lambda_i$ fixing $c_i$, and subsequently solve for $c_i$ fixing $\phi$ and $\lambda_i$. This procedure is iterated to convergence.

We chose to use the above simpler procedure in favor of a Newton iteration for the following reasons. There two major nonlinearities in the equations: the drift term in the drift-diffusion equation and the ion channel current terms in the membrane boundary conditions. The drift term couples the concentration term $c_i$ with the gradient of the electrostatic potential. Suppose there are $N_{\mathrm{fv}}$ FVs and $N(=3,4$ in computational runs presented in Section 7 but potentially much larger) ionic species of interest. A Newton iteration will require solution of a nonsymmetric linear system with $N_{\mathrm{fv}} \times (N+1)$ unknowns at each iterative step. In the simpler procedure to be explained below, all linear systems are positive symmetric (semi)definite with

$N_{\mathrm{fv}}$ unknowns. The complicated dependence of ion channel current terms on $c_i$ and $\phi$ add further algebraic complications in generating the Jacobian matrix needed at each iteration. A possible future direction is to use the simpler solution iterative procedure adopted here as a preconditioner in a Jacobian-free Newton–Krylov framework [17].

Let $c_i^{p,n,m}$, $\phi^{p,n,m}$, $\lambda_i^{(p,p'),n,m}$ denote the $m$-th iterate of the solution procedure, where $m = 0, 1, 2, \ldots$. We set our initial iterate for each variable to be equal to the value of that variable at time step $n-1$:

$$c_i^{p,n,0} = c_i^{p,n-1}, \quad \phi^{p,n,0} = \phi^{p,n-1}, \quad \lambda_i^{(p,p'),n,0} = \lambda_i^{(p,p'),n-1}. \tag{40}$$

We first solve for $\phi^{p,n,m}$. We take (39) and fix the ionic concentrations to their values at the previous iteration step $c_i = c_i^{n,m-1}$ so that the only unknown is $\phi^{n,m}$.

$$\begin{aligned} -\frac{\rho_0^p + \sum_{i=1}^N q z_i c_i^{p,n-1}}{\Delta t} = & \\ & -\frac{1}{V_p}\sum_{p'\neq p} e^{(p,p')} \sum_{i=1}^N q z_i F_i^{(p,p')}(c_i^{n,m-1}, \phi^{n,m}) \\ & -\frac{1}{V_p}\sum_{p'\neq p} \gamma^{(p,p')} C_m \Big(\frac{\phi_{\mathrm{m}}^{(p,p'),n,m} - \phi_{\mathrm{m}}^{(p,p'),n-1}}{\Delta t}\Big) \\ & -\frac{1}{V_p}\sum_{p'\neq p} \gamma^{(p,p')} \sum_i j_i^{(p,p'),n,m}(s^{n,m}, \phi_{\mathrm{m}}^{(p,p'),n,m}, c^{n-1}). \end{aligned} \tag{41}$$

By evaluating $c_i$ at $c_i^{n,m-1}$ in the flux term $F_i^{(p,p')}$, we avoid dealing with the nonlinearity that arises from the drift term. The only possibility for a nonlinearity in the above is in the transmembrane current term. In many applications, $j_i$ is assumed linear in $\phi_{\mathrm{m}}$. If not, we linearize as follows:

We first recall the functional form of transmembrane current terms. The general functional form of ion channel currents is written as

$$j_i = \sum_\alpha j_{i,\alpha}, \quad j_{i,\alpha} = g_{i,\alpha}(\boldsymbol{x}, s, \phi_{\mathrm{m}}, c^{(k)}, c^{(l)}) \mathcal{J}_{i,\alpha}(\phi_{\mathrm{m}}, c_i^{(k)}, c_i^{(l)}), \tag{42}$$

where $\alpha$ labels the types of ion channels present, and $j_{i,\alpha}$ the transmembrane current through ion channels of this type. $g_{i,\alpha}$ is the density of the such open ion channels per unit area of membrane, and $\mathcal{J}_{i,\alpha}$ is the instantaneous current voltage relationship of a single open channel. We choose a suitable linearization of the instantaneous current voltage relation with respect to $\phi_{\mathrm{m}}^{(p,p')}$ around $\phi_{\mathrm{m}}^{(p,p'),n,m-1}$:

$$\mathcal{J}^L_{i,\alpha}(\phi_{\mathrm{m}}^{(p,p'),n,m}, c_i^p, c_i^{p'}) = \mathcal{D}_{\mathcal{J}_{i,\alpha}}(\phi_{\mathrm{m}}^{p,n,m-1}, c_i^p, c_i^{p'})(\phi_{\mathrm{m}}^{(p,p'),n,m} - \phi_{\mathrm{m}}^{(p,p'),n,m-1}) + \mathcal{J}_{i,\alpha}(\phi_{\mathrm{m}}^{(p,p'),n,m-1}, c_i^{p'}, c_i^{p'}). \quad (43)$$

The term $\mathcal{D}_{\mathcal{J}_{i,\alpha}}$ will typically be the derivative of $I_{i,\alpha}$ with respect to $\phi^{\mathrm{m}}$. Instead of $j_i$ itself, we shall therefore use the following linearization in its place in (41).

$$\begin{aligned} j_i^{L,p,n,m} &= \sum_\alpha j_{i,\alpha}^{L,p,n,m}, \\ j_{i,\alpha}^{L,n,p,m} &= g_{i,\alpha}(s^{(p,p'),n}, \phi_{\mathrm{m}}^{(p,p'),n-1}, c^{n-1})\mathcal{J}^L_{i,\alpha}(\phi_{\mathrm{m}}^{(p,p'),n,m}, c_i^{n-1}). \end{aligned} \quad (44)$$

Note that $s^{(p,p'),n}$ is already a known quantity; we do not have to solve for it.

The result is a linear equation in $\phi$, which can now be solved.

Solving for $\lambda_i^{(p,p'),n,m}$ is simple:

$$\frac{\lambda_i^{(p,p'),n,r} - \lambda_i^{(p,p'),n-1}}{\Delta t} = \frac{\tilde{\lambda}_i^{(p,p'),n,m-1} - \lambda_i^{(p,p'),n,m}}{r_d^2/D_0}, \quad (45)$$

where $\tilde{\lambda}_i^{(p,p'),n,m-1}$ is evaluated using $c_i^{p,n,m-1}$.

Given $\phi^{p,n,m}$ and $\lambda_i^{(p,p'),n,m}$, we solve for $c_i^{p,n,m}$ as follows:

$$\frac{c_i^{p,n,m} - c_i^{p,n-1}}{\Delta t} = -\frac{1}{V_p}\sum_{p' \neq p}(e^{(p,p')}F_i^{(p,p'),n,m} + \gamma^{(p,p')}G_i^{(p,p'),n,m}), \quad (46)$$

where the flux density expressions are given by

$$\begin{aligned} F_i^{(p,p'),n,m} &= D_i\Big(\frac{c_i^{p,n,m} - c_i^{p',n,m}}{h}\Big) \\ &\quad + D_i\frac{qz_i}{k_BT}\Big(\frac{c_i^{p,n,m-1} + c_i^{p',n,m-1}}{2}\Big)\Big(\frac{\phi^{p,n,m-1} - \phi^{p',n,m-1}}{h}\Big), \quad (47) \\ qz_iG_i^{(p,p'),n,m} &= C_{\mathrm{m}}\Big(\frac{\lambda_i^{(p,p'),n,m}\phi_{\mathrm{m}}^{(p,p'),n,m} - \lambda_i^{(p,p'),n-1}\phi_{\mathrm{m}}^{(p,p'),n-1}}{\Delta t}\Big) + j_i^{(p,p'),n,m}, \end{aligned}$$

where the flux expression (47) is to be suitably modified when dealing with nonuniform meshes; see (29). In the above (47), the diffusive flux is treated implicitly, whereas drift flux is left explicit. The rationale for this difference in treatment of the two flux terms is that the diffusive flux involves derivatives of $c_i$ but the drift flux does not.

With the above expression for $F_i^{(p,p'),n,m}$, (46) is a linear equation in $c_i$. In fact, this is just a familiar discretization of the diffusion equation with a source term and flux boundary conditions.

We now iterate this procedure in $m$ a suitable number of times, and set the final iterate to be the values at time $n$. Note that one iteration is enough to obtain a first order scheme in time. We also point out that the scheme is conservative in exact arithmetic: we have ion conservation regardless of how may iterations we perform.

We iterate so that electroneutrality is better satisfied at time $n$. Multiplying (46) with $qz_i$ and summing in $i$ does not reproduce (41) because the concentrations in the flux approximation $F_i^q$ are evaluated using different values in the two expressions. Therefore, the solution to (46) only satisfies electroneutrality in the limit $m \to \infty$.

Our termination criterion for the above iteration is to check whether the electroneutrality condition is satisfied to within a certain tolerance after the $r$-th iteration. We use the following criterion:

$$\frac{\sum_p V_p |\rho_0 + \sum_i q z_i c_i^{p,n,m}|}{\sum_p V_p} < \epsilon_{\text{tol}} q c_0. \tag{48}$$

In all computations, we take $\epsilon_{\text{tol}} = 1 \times 10^{-5}$ and $c_0 = 100\,\text{mmol/l}$, the typical ionic concentration. We set this final iterate to be the value of $c_i$, $\phi$ at the next time step, except for the adjustment we discuss below.

When we use no-flux boundary conditions at the outer rim of the computational domain, we perform the following adjustment at the end of each computational step, in order to correct for the nonconservation of ions that is purely the result of round-off error. We fix the concentrations so that the global amount of each ionic species is conserved as strictly as possible by setting

$$c_i^{p,n} = \left( \frac{Q_i^{\text{init}} - \Lambda_i^{n,m}}{Q_i^{n,m}} \right) c_i^{p,n,m}, \tag{49}$$

where

$$Q_i^{n,m} = \sum_p V_p c_i^{p,n,m}, \qquad \Lambda_i^{n,m} = \frac{1}{q z_i} \sum_{(p,p'),p \neq p'} \gamma^{(p,p')} \lambda_i^{(p,p'),n,m} C_{\text{m}} \phi_{\text{m}}^{(p,p'),n,m}.$$

The summation in the definition of $\Lambda_i^{n,m}$ is over all ordered pairs $(p, p')$. The index $m$ denotes the final iterate, that is, the result before this adjustment is made. The term $Q_i^{\text{init}}$ is the total amount of the $i$-th ion at the initial time:

$$Q_i^{\text{init}} = \sum_p V_p c_i^{p,0} + \frac{1}{q z_i} \sum_{(p,p'),p \neq p'} \gamma^{(p,p')} \lambda_i^{(p,p'),0} C_{\text{m}} \phi_{\text{m}}^{(p,p'),0}. \tag{50}$$

The first sum represents the ions in the bulk solution, whereas the second term is the contribution from the membrane surface charge.

Why do we need to perform this fix when we know that the scheme is in fact conservative? The unfortunate reality, however, is that the scheme is conservative

only in exact arithmetic. With floating point arithmetic, errors tend to accumulate and, with time, ion conservation is violated. Computational experiments indicate that this error is negligible as far as the values of $c_i$ are concerned. This has to be corrected nonetheless because this small violation leads to global charge accumulation, which in turn leads to nonconvergence of Krylov iterations for $\phi$ when no-flux boundary conditions are used (for no-flux boundary conditions, we perform Krylov iterations in the subspace spanned by all grid functions that integrate to 0 over the spatial domain, and global charge accumulation leads to nonexistence of solutions, as can be seen by considering the Fredholm alternative). The scheme presented above has an inherent mechanism to eliminate *local* charge accumulation (39), but cannot eliminate *global* charge accumulation. The above adjustment is on the order of round-off error at each time step.

We note that this fix is only necessary for the no-flux boundary condition. When Dirichlet or mixed boundary conditions are imposed at the outer rim of the computational domain, global accumulation in charge in the computational domain will eventually dissipate through communication with the outer bath.

The solution to the nonlinear algebraic equations requires the solution of a linear system at each iteration. We note that solving for the electrostatic potential as well as the concentrations involve solving a positive definite symmetric system. We thus either use a direct solver(Cholesky decomposition) or the conjugate gradient method [36]. The code for cylindrical geometry has been implemented using Matlab, where we use a direct solver. The code for general two-dimensional geometry has been written in C++, where we use PETSc for the linear algebra routines [2]. PETSc is a package that provides sparse linear solvers and is designed to be suitable for parallel algorithms. Although we do not yet use parallel machines, having coded in PETSc should facilitate this transition in the future.

## 7. Convergence study: cylindrical geometry

We test the convergence for the cylindrical case for two kinds of situations, the standard Hodgkin–Huxley axon [11; 16; 18], and for a cardiac model of ephaptic coupling.

**7.1.** ***Hodgkin–Huxley axon.*** The neuronal axon is the standard biological system to which the cable model is applied. We take this system as our first test case.

For ionic channel parameters, we shall use those of the standard Hodgkin–Huxley model. There are several parameters that are required for computation with the electroneutral model but not with the cable model. They are the diffusion coefficients for each ionic species and the initial concentration of the ions. We consider three ionic species $Na^+$, $Cl^-$, and $K^+$. The initial concentrations and the diffusion coefficients we use are listed in Table 1. The membrane charge ratios $\lambda_i$

| | | |
|---|---|---|
| $T$ | Absolute temperature | $273.15+37$ K |
| $D_{Na^+}$ | Diffusion coefficient of $Na^+$ | $1.33\,\mu m^2/ms$ [18] |
| $D_{K^+}$ | Diffusion coefficient of $K^+$ | $1.96\,\mu m^2/ms$ [18] |
| $D_{Cl^-}$ | Diffusion coefficient of $Cl^-$ | $2.03\,\mu m^2/ms$ [18] |
| $c^{int}_{Na^+}\big\vert_{t=0}$ | Initial intracellular concentration of $Na^+$ | 10 mmol/l |
| $c^{ext}_{Na^+}\big\vert_{t=0}$ | Initial extracellular concentration of $Na^+$ | 145 mmol/l |
| $c^{int}_{K^+}\big\vert_{t=0}$ | Initial intracellular concentration of $K^+$ | 140 mmol/l |
| $c^{ext}_{K^+}\big\vert_{t=0}$ | Initial extracellular concentration of $K^+$ | 5 mmol/l |
| $c^{int}_{Cl^-}\big\vert_{t=0}$ | Initial intracellular concentration of $Cl^-$ | 150 mmol/l |
| $c^{ext}_{Cl^-}\big\vert_{t=0}$ | Initial extracellular concentration of $Cl^-$ | 150 mmol/l |
| $\phi_m\vert_{t=0}$ | Initial transmembrane potential, $\phi^{int}-\phi^{ext}$ | $-70$ mV |

**Table 1.** Parameter values used in the Hodgkin–Huxley simulations of the axon.

are initialized so that $\lambda_i\big\vert_{t=0} = \tilde{\lambda}_i\big\vert_{t=0}$. The immobile charge density was taken so that electroneutrality is satisfied at each spatial point at $t = 0$. The Hodgkin–Huxley model has one free parameter, the value of the equilibrium potential [16], which we take to be $-70$ mV. The initial value of the gating variables are set to the equilibrium values at $-70$ mV.

We take the axon to be a cylinder of radius $l\,\mu$m and axial length $l_A\,\mu$m. Take the $z$ axis along the axis of the cylinder, with the axonal ends at $z = \pm l_A/2$, and the radial axis $r$ from the center of the cylinder. The cylindrical axon is bathed in an extracellular medium located between the cell membrane at $r = l$ and $r = 2l$, where we impose no-flux boundary conditions. We also impose no-flux boundary conditions at $z = \pm l_A/2$. The total simulation time be $T_e$. We choose the diameter $2l$ and the axial length $l_A$ to be

$$2l = 0.1, 1, 10\,\mu\text{m}, \quad l_A = 4\sqrt{2l}\times 10^3\,\mu\text{m}, \quad T_e = 4\,\text{ms}. \tag{51}$$

We note that the axonal length is much greater than the radial length. This length of the axon $l_A$ was chosen so that we can see a wave of propagating action potential. This choice also roughly corresponds to the action propagation speed seen in unmyelinated neuronal axons on the order of 10 mm/ms at an axonal diameter of 1–10 $\mu$m. We use the above dependence of $l_A$ on $l$ since, according to cable theory, the electrotonic length (the typical length scale for the spread of membrane potential) scales with the square root of the axonal diameter.

At time $t = 0$, we initiate an action potential by transiently increasing the $Cl^-$ conductance, for which we specify the following spatial distribution and time dependence:

$$G_{Cl^-} = \begin{cases} 5\left(1+\cos\frac{12\pi z}{l_A}\right)\left(1-\cos\frac{2\pi t}{T_s}\right) & \text{if } -\frac{l_A}{12} < z < \frac{l_A}{12},\ t < T_s = 1\,\text{ms}, \\ 0 & \text{otherwise.} \end{cases}$$

We thus give a brief change in the membrane chloride conductance at the center of the axon. An action potential is initiated here and spreads towards the two ends of the axon. A snapshot from a sample run where the diameter $2l = 1\ \mu$m is shown in Figures 4 and 5.

In the case of the cylindrical axon, the computational runs exhibit little radial variation in the electrostatic potential, and one may argue against the use of this computationally intensive model in place of much simpler models such as the cable model. In Section 7.2, we shall see a case in which a radial variation in the electrostatic potential is seen. Even in the case of a cylindrical axon, however, we

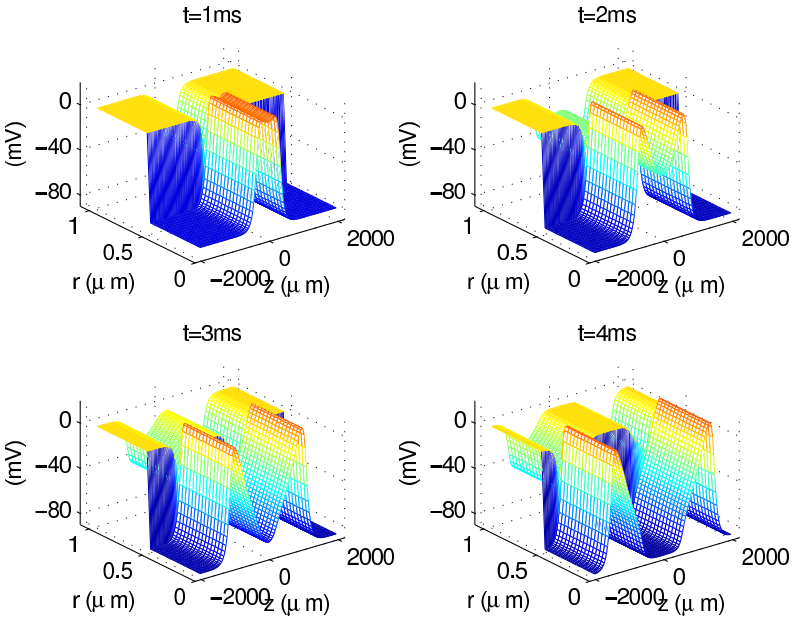


**Figure 4.** Electrostatic potential $\phi$ at $t = 1, 2, 3, 4$ ms, $2l = 1\ \mu$m. Since the solutions we seek are radially symmetric, the radial cross-section ($r$ between 0 $\mu$m and 1 $\mu$m) is plotted in the graph. The jump discontinuity at $r = 0.5\ \mu$m signifies the jump in the electrostatic potential. The mesh size is $N_z \times N_r = 128 \times 32$. Potential is measured in mV and length in $\mu$m.

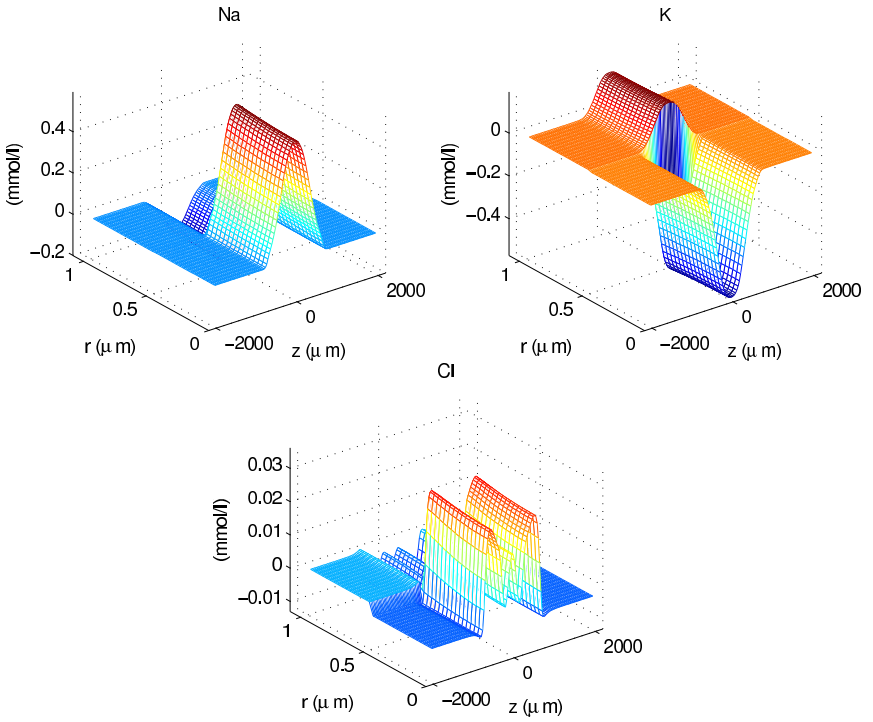


**Figure 5.** Cumulative *change* in ionic concentrations from $t = 0$ at $t = 2$ ms, $2l = 1$ $\mu$m. The cumulative concentration changes in $Na^+$, $K^+$, and $Cl^-$ are shown. As with the previous figure, the radial cross section is plotted. The mesh size is $N_z \times N_r = 128 \times 32$. Concentration is measured in mmol/l and length in $\mu$m.

believe that this model can be useful in the following respects. First, it allows us to track ionic concentration, whose evolution cannot be determined without solving for the electrostatic potential which ensures that electroneutrality be satisfied pointwise in space. The constraint of electroneutrality may give rise not only to quantitative but also qualitatively different behavior compared to simple diffusion [32]. Second, this model can be used as a validation tool to judge when the cable model is a good approximation [18; 33]. We hope to make a more detailed comparison between the cable model and our model in a future publication.

*Convergence in space.* We take a uniform grid of $N_z \times N_r$ over the simulation domain. We set

$$N_z = 64 \times 2^{n-1}, \quad N_r = 16 \times 2^{n-1}, \quad \Delta t = 0.02\,\text{ms}, \quad N_T = \frac{T_e}{\Delta t} = 200, \quad (52)$$

where $n = 1, \ldots, 4$. Note that here and throughout the paper the time step remains fixed in our spatial convergence studies. The possibility of proceeding in this way without encountering numerical instability is conceptually related to the unconditional stability of our implicit computational scheme. During spatial grid refinement, the bounds on spatial difference operators grow because of the appearance of the mesh width in the denominators of the difference operators. This reflects the unbounded nature of the corresponding differential operators. In an explicit scheme, the growth of the operator norms needs to be compensated by refinement of the time step, but we do not have to do that here.

To measure the convergence rate, we define the discrete $p$-norm as

$$\|u\|_{L^p} = \Big(\sum_{k=1}^{2N_r} |V_k||u_k|^p\Big)^{1/p}, \quad 1 \le p < \infty, \quad \|u\|_{L^\infty} = \max_k |u_k|. \tag{53}$$

The convergence rate is measured by comparing the interpolation of the numerical solution at a finer level to the numerical solution at a coarser level. Let $c_i$ computed with an $N_r \times N_r$ mesh be written as $c_i^{N_r}$. We define a measure of error $e_p^s[c_i; N_r]$ as follows.

$$e_p^s[c_i; N_r] = \big\| c_i^{N_r} - \mathcal{I}^{2N_r \to N_r} c_i^{2N_r} \big\|_{L^p}. \tag{54}$$

Here, $\mathcal{I}^{2N_r \to N_r}$ is an interpolation operator from the finer to the coarser grid.

For the electrostatic potential $\phi$, we need to take into account the arbitrariness of $\phi$, up to addition of a constant. Thus, we measure the error in $\phi$ as

$$e_p^s[\phi; N_r] = \min_{c_\phi \in \mathbb{R}} \big\| \phi^{N_r} - \mathcal{I}^{2N_r \to N_r} \phi^{2N_r} - c_\phi \big\|_{L^p}. \tag{55}$$

As an empirical measure of convergence rate in space, we use

$$r_p^s[\psi; N_r] = \log_2\Big(\frac{e_p^s[\psi; N_r]}{e_p^s[\psi; 2N_r]}\Big), \tag{56}$$

where $\psi$ can be either $c_i$ or $\phi$.

Table 2 lists the rate of convergence for both $c_i$ and $\phi$ at the three diameters with three norms, $L^1$, $L^2$ and $L^\infty$, at time $t = 4$ ms. Convergence rates at other time points were similar.

We see second order convergence for most parameter regions considered. The second order convergence observed here is, however, lost in the case of general two-dimensional geometry (Section 8). This favorable property is thus tied to the fact that the membrane geometry conforms to the underlying Cartesian grid. The deterioration in convergence rate when the axonal diameter is equal to 10 $\mu$m seems attributable to the fact that the concentration gradients near the membrane are not fully resolved when $N_r = 32$. Since the mesh has been scaled with the axon size, the largest axon also has the coarsest mesh, in absolute terms. This affects the

| diameter | norm | $r_p^s[c_1, 32]$ | $r_p^s[c_2, 32]$ | $r_p^s[c_3, 32]$ | $r_p^s[\phi, 32]$ |
|---|---|---|---|---|---|
| 0.1 | $L^1$ | 1.97 | 1.97 | 1.93 | 1.96 |
| | $L^2$ | 1.97 | 1.97 | 1.94 | 1.98 |
| | $L^\infty$ | 1.97 | 1.97 | 1.78 | 1.90 |
| 1 | $L^1$ | 1.97 | 1.97 | 1.93 | 1.96 |
| | $L^2$ | 1.97 | 1.97 | 1.95 | 1.97 |
| | $L^\infty$ | 1.97 | 1.97 | 1.88 | 1.82 |
| 10 | $L^1$ | 1.97 | 1.97 | 1.92 | 1.97 |
| | $L^2$ | 1.96 | 1.97 | 1.84 | 1.98 |
| | $L^\infty$ | 1.44 | 1.80 | 1.41 | 1.82 |

**Table 2.** Convergence rate in space ($r_p^s$) for different axonal diameters. Values computed at $t = 4$ ms, and $N_r = 32$.

quality of the computed solution because the radial concentration profiles do *not* scale with the size of the axon.

*Convergence in time.* Convergence in time is measured similarly to the spatial case. We vary the time step so that

$$\Delta t = 0.04 \times 2^{1-n}, \quad N_T \equiv \frac{T_e}{\Delta t} = 100 \times 2^{n-1}, \tag{57}$$

where $n = 1, \ldots, 4$. We take $N_r = 32$ as our spatial grid to assess time convergence.

The convergence rate and error is computed analogously to the spatial case.

$$e_p^t[c_i; N_r] = \left\| c_i^{N_T} - \mathcal{I}^{2N_T \to N_T} c_i^{2N_T} \right\|_{L^p}. \tag{58}$$

Here, $\mathcal{I}^{2N_T \to N_T}$ is an interpolation operator from the finer to the coarser time step. For the electrostatic potential $\phi$, we let

$$e_p^t[\phi; N_T] = \min_{c_\phi \in \mathbb{R}} \left\| \phi^{N_T} - \mathcal{I}^{2N_T \to N_T} \phi^{2N_T} - c_\phi \right\|_{L^p}. \tag{59}$$

As an empirical measure of convergence rate in time, we use

$$r_p^t[\psi; N_T] = \log_2 \frac{e_p^t[\psi; N_T]}{e_p^t[\psi; 2N_T]}. \tag{60}$$

where $\psi$ can be either $c_i$ or $\phi$.

Table 3 lists the rate of convergence for both $c_i$ and $\phi$ at the three diameters with three norms, $L^1$, $L^2$ and $L^\infty$ at $t = 4$ ms. We see approximate first order convergence in time over all parameter ranges considered, although the convergence rate is slightly sublinear overall. The source of this sublinear convergence rate is unclear.

| diameter | norm | $r_p^t[c_1, 200]$ | $r_p^t[c_2, 200]$ | $r_p^t[c_3, 200]$ | $r_p^t[\phi, 200]$ |
|---|---|---|---|---|---|
| 0.1 | $L^1$ | 0.93 | 0.93 | 0.93 | 0.92 |
| | $L^2$ | 0.94 | 0.94 | 0.90 | 0.89 |
| | $L^\infty$ | 0.96 | 0.96 | 0.90 | 0.83 |
| 1 | $L^1$ | 0.93 | 0.93 | 0.93 | 0.92 |
| | $L^2$ | 0.94 | 0.94 | 0.89 | 0.89 |
| | $L^\infty$ | 0.95 | 0.96 | 0.75 | 0.81 |
| 10 | $L^1$ | 0.93 | 0.93 | 0.91 | 0.92 |
| | $L^2$ | 0.93 | 0.94 | 0.86 | 0.89 |
| | $L^\infty$ | 0.77 | 0.95 | 0.75 | 0.82 |

**Table 3.** Convergence rate in time ($r_p^t$) for different axonal diameters. Values computed at $t = 4$ ms, and $N_T = 200$.

*Convergence in space and time.* We next refine in both space and time to demonstrate that the approximation approaches the solution to the PDE system. Given that we observe second order convergence in space and first order convergence in time, we should be able to observe second order convergence overall if we make the time step proportional to the square of the mesh width. We let

$$N_z = 4 \times N_r, \quad N_r = 32 \times 2^{n-1}, \quad \Delta t = 0.02 \times 4^{1-n}, \quad N_T \equiv \frac{T_e}{\Delta t} = 200 \times 4^{n-1},$$

for $n = 1, \ldots, 3$. The spatiotemporal convergence rate $r_p^{st}$ is measured similarly to the empirical spatial and temporal rates $r_p^s$ and $r_p^t$ defined in (56) and (60). Table 4 exhibits approximate second order convergence overall.

| diameter | norm | $r_p^{st}[c_1, 32]$ | $r_p^{st}[c_2, 32]$ | $r_p^{st}[c_3, 32]$ | $r_p^{st}[\phi, 32]$ |
|---|---|---|---|---|---|
| 0.1 | $L^1$ | 1.94 | 1.94 | 1.93 | 1.93 |
| | $L^2$ | 1.93 | 1.95 | 1.89 | 1.90 |
| | $L^\infty$ | 1.95 | 1.95 | 1.80 | 1.86 |
| 1 | $L^1$ | 1.94 | 1.94 | 1.93 | 1.93 |
| | $L^2$ | 1.94 | 1.95 | 1.89 | 1.90 |
| | $L^\infty$ | 1.95 | 1.96 | 1.82 | 1.86 |
| 10 | $L^1$ | 1.94 | 1.94 | 1.90 | 1.93 |
| | $L^2$ | 1.93 | 1.94 | 1.82 | 1.90 |
| | $L^\infty$ | 1.57 | 1.87 | 1.50 | 1.86 |

**Table 4.** Convergence rate in space and time ($r_p^{st}$) for different values of axonal diameters. Values computed at $t = 4$ ms, and $N_r = 32$, $N_T = 200$.

**7.2.** ***Cardiac geometry.*** We next consider a test geometry based on cardiac microscopic anatomy [35; 19; 26]. The motivation for this test case is the following. Cardiac tissue is composed of muscle cells which are linked to one another through gap junctions, pore forming proteins similar to ion channels that straddle two adjacent cell membranes. These low resistance passage ways of electric current have conventionally been regarded as essential for successful cell-to-cell propagation of the cardiac electric signal, which in turn coordinates the synchronization of the heart beat [31]. Recent experimental as well as theoretical studies suggest, however, that gap junctions are not absolutely essential for propagation of the electric signal. Indeed, knock-out mice that do not express the principal gap junction isoforms in cardiac cells do produce a functional heart beat [37; 9]. One hypothesis that attempts to explain this anomalous conduction is the ephaptic hypothesis, in which two adjacent cardiac cells interact with one another through the very narrow cleft (the intercalating disc) between them [19]. The presence of the narrow cleft raises the possibility of steep voltage gradients and large ionic concentration changes, and is thus an ideal system in which our model could make interesting physiological predictions. This program has been partially carried out in [26], to which we refer the reader for further physiological discussion.

As a testbed, we consider 2 cells of equal length separated by a narrow intercellular space of width $l_g$. In fact, we consider two "half" cells, each of length $l_A/2$ as we shall see shortly. The radius of the cell is $l$ and the whole system is bathed in an extracellular medium contained within a cylinder of radius $2l$ (Figure 6).

Similarly to the axonal case, we take $z$ to be the axial direction and $r$ to be the radial coordinate. We take the origin to be in the middle of the gap. Formally, the intracellular region can be written as

$$\left(-\frac{l_A+l_g}{2} < z < -\frac{l_g}{2} \quad \text{or} \quad \frac{l_g}{2} < z < \frac{l_A+l_g}{2}\right) \quad \text{and} \quad r < l. \tag{61}$$

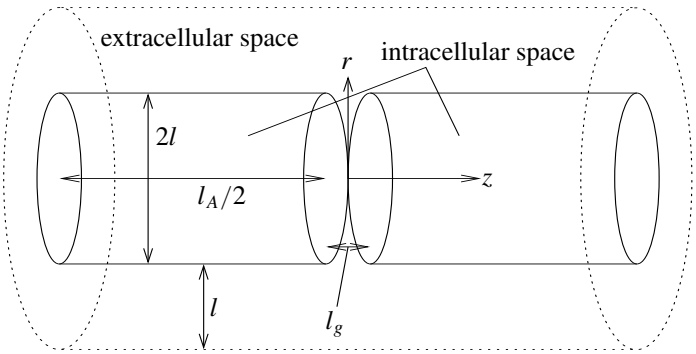


**Figure 6.** Schematic of the geometry used for the cardiac model.

| | | |
|---|---|---|
| $T$ | Absolute temperature | $273.15+37$ K |
| $D^{\text{us}}_{\text{Na}^+}$ | Unscaled diffusion coefficient of $Na^+$ | $1.33\ \mu m^2/ms$ |
| $D^{\text{us}}_{\text{K}^+}$ | Unscaled diffusion coefficient of $K^+$ | $1.96\ \mu m^2/ms$ |
| $D^{\text{us}}_{\text{Ca}^{2+}}$ | Unscaled diffusion coefficient of $Ca^{2+}$ | $0.3\ \ \mu m^2/ms$ |
| $D^{\text{us}}_{\text{Cl}^-}$ | Unscaled diffusion coefficient of $Cl^-$ | $2.03\ \mu m^2/ms$ |
| $c^{\text{int}}_{\text{Na}^+}\big\vert_{t=0}$ | Initial intracellular concentration of $Na^+$ | 10 mmol/l |
| $c^{\text{ext}}_{\text{Na}^+}\big\vert_{t=0}$ | Initial extracellular concentration of $Na^+$ | 145 mmol/l |
| $c^{\text{int}}_{\text{K}^+}\big\vert_{t=0}$ | Initial intracellular concentration of $K^+$ | 140 mmol/l |
| $c^{\text{ext}}_{\text{K}^+}\big\vert_{t=0}$ | Initial extracellular concentration of $K^+$ | 5 mmol/l |
| $c^{\text{int}}_{\text{Cl}^-}\big\vert_{t=0}$ | Initial intracellular concentration of $Cl^-$ | 10 mmol/l |
| $c^{\text{ext}}_{\text{Cl}^-}\big\vert_{t=0}$ | Initial extracellular concentration of $Cl^-$ | see text |
| $c^{\text{int}}_{\text{Ca}^{2+}}\big\vert_{t=0}$ | Initial intracellular concentration of $Ca^{2+}$ | 0.4 $\mu$mol/l |
| $c^{\text{ext}}_{\text{Ca}^{2+}}\big\vert_{t=0}$ | Initial extracellular concentration of $Ca^{2+}$ | 2 mmol/l |
| $\phi_m\vert_{t=0}$ | Initial transmembrane potential, $\phi^{\text{int}}-\phi^{\text{ext}}$ | $-90$ mV |

**Table 5.** Parameter values used in cardiac simulation.

The intracellular region is open-ended at $z=\pm\frac{1}{2}(l_A+l_g)$. This is what we mean by "half cell". We impose no-flux boundary conditions at $z=\pm\frac{1}{2}(l_A+l_g)$ and at $r=2l$.

The values for $l_g$, $l_A$ and $l$ are

$$l_g=20\,\text{nm},\quad l_A=100\,\mu\text{m},\quad l=11\,\mu\text{m}. \tag{62}$$

We note that $l_g$ is about 4 orders of magnitude smaller than $l_A$, and thus we use a nonuniform mesh, the details of which we shall describe shortly.

We consider 4 ion types in the calculation, $Na^+$, $K^+$, $Ca^{2+}$ and $Cl^-$. The initial condition for all ionic species except $Cl^-$ in the extracellular space are listed in Table 5. In the intracellular medium, we set the fixed negative charge density $\rho_0$ so that electroneutrality is satisfied everywhere. In the gap we introduce a nonuniform fixed negative charge density. This represents the charged groups on extracellular macromolecules that may be present within the gap. We initialize the fixed charge density $\rho_0$ in the extracellular space to be

$$\rho_0=\begin{cases}-\big(54+50\big(1-(r/l)^2\big)\big)\ \text{mmol/l} & \text{if } r<l \text{ and } -l_g/2<z<l_g/2,\\ -54\ \text{mmol/l} & \text{if } r\geq l.\end{cases}$$

Set the extracellular $Cl^-$ concentration so that the electroneutrality condition is satisfied everywhere:

$$c^{\text{ext}}_{Cl^-}\big|_{t=0} = \begin{cases} 100 - 50\big(1 - (r/l)^2\big)\,\text{mmol/l} & \text{if } r < l \text{ and } -l_g/2 < z < l_g/2, \\ 100\,\text{mmol/l} & \text{if } r \geq l. \end{cases}$$

The diffusion coefficients are adjusted in the following way. If we ignore ionic diffusion, electric current is solely driven by the gradient of the electrostatic potential. In this case, the ohmic cytoplasmic conductance is given by $a(\boldsymbol{x}, t)$ defined in (5). If one computes the cytoplasmic or extracellular conductance using (5) according to values of $D_i$ in an aqueous solution, the values used in Table 1, we obtain an overestimate which deviates from the experimentally observed value by a factor of 2–5 [19]. We thus scale the diffusion coefficient in aqueous solution by a uniform factor $\alpha$ so that the cytoplasmic or extracellular conductance calculated above is approximately within the experimental range. More concretely, we let

$$g^{\text{observed}} = \alpha \overline{\sum_{i=1}^{N} \frac{(q z_i)^2\, c_i|_{t=0}}{k_B T} D_i^{\text{us}}}, \tag{63}$$

where $g^{\text{observed}}$ is the cytoplasmic conductance, which we take to be equal to the extracellular conductance, $D_i^{\text{us}}$ is the unscaled diffusion coefficient, and overline denotes averaging over the computational domain. Following [19], we let $1/g^{\text{observed}} = 150\,\Omega\,\text{cm}$.

For the ion channel composition for the membrane, we use the model of Bernus et al. [4], in which the authors model the electrical activity of human ventricular myocytes. The only change we make concerns the localization of the $Na^+$ channels. We concentrate their distribution so that 99% of the total $Na^+$ conductance sits at the membranes facing the gap. Evidence for such localization of $Na^+$ channel expression has been presented in [19]. This may allow an action potential to propagate across the gap without the two intracellular spaces being directly connected by gap junctions forming a cytoplasmic bridge.

All instantaneous current voltage relations for ionic channels in the model of Bernus et al. are linear in the transmembrane voltage. We do not have to linearize the current voltage relationship to obtain a linear system. The ionic pump currents are nonlinear in the transmembrane voltage, but will be treated explicitly. This does not result in numerical instabilities because ionic pump currents are typically small in magnitude.

We simulate this system for time $T_e = 4\,\text{ms}$. We add a transient excitation to the system by way of an increase in $Na^+$ conductance distributed along the lateral cell membrane of the cell on the left according to

$$G_{\mathrm{Na}^+}^{\mathrm{add}} = \begin{cases} \frac{5}{4}\left(1+\cos\frac{\pi(z+L_z)}{l_A/2}\right)\left(1-\cos\frac{2\pi t}{\tau_e}\right) & \text{if } z < -\frac{l_g}{2},\ t < \tau_e, \\ 0 & \text{otherwise,} \end{cases}$$

where $L_z = (l_A + l_g)/2$ and $\tau_e = 1$ ms. Thus, we stimulate the system at one end of the cell located in $z < 0$, and see whether the action potential propagates into the next cell. Snapshots from this simulation are shown in Figures 7 and 8. We note a radial gradient in the electrostatic potential in the thin gap spaces, an effect that cannot be modeled with a simple use of the cable model. Note in these figures that the action potential propagates across a thin gap between two cells even if there are no gap junctions (low resistance connections) that connect the two cells. The feasibility of such *ephaptic* transmission (a term borrowed from neuroscience [12]), in the context of cardiac action potential propagation has been a subject of much debate [19; 35]. We have used this model to explore the biophysics of this mechanism in [26].

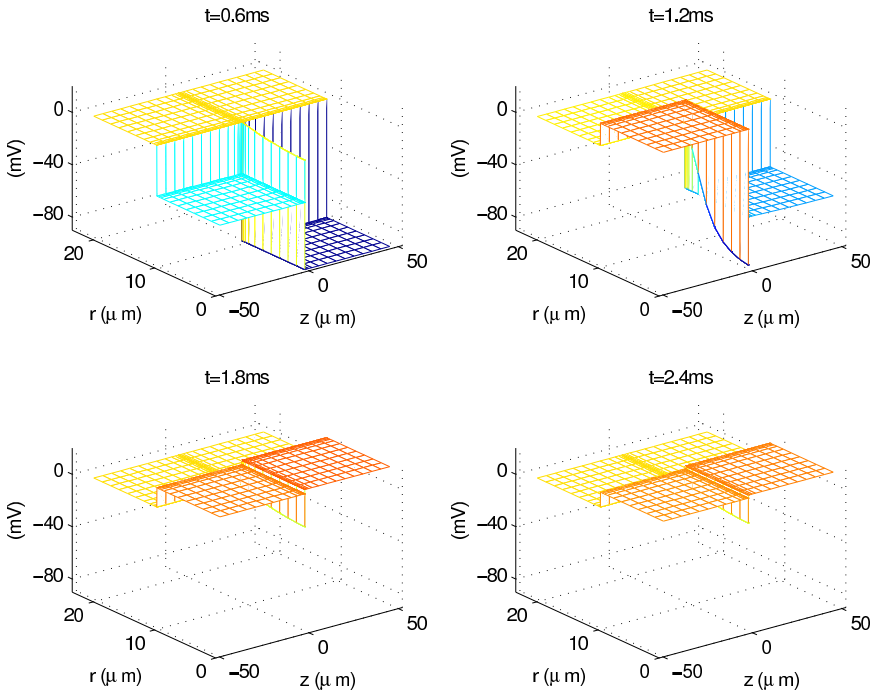


**Figure 7.** The evolution of the electrostatic potential in the cardiac simulation with variable mesh width. The radial cross section ($r$ from 0 $\mu$m to 20 $\mu$m) is shown. Snapshots shown at $t = 0.6, 1.2, 1.8, 2.4$ ms. The mesh size is $N_z \times N_r = 48 \times 32$ in this computation. Potentials are in mV and lengths in $\mu$m.

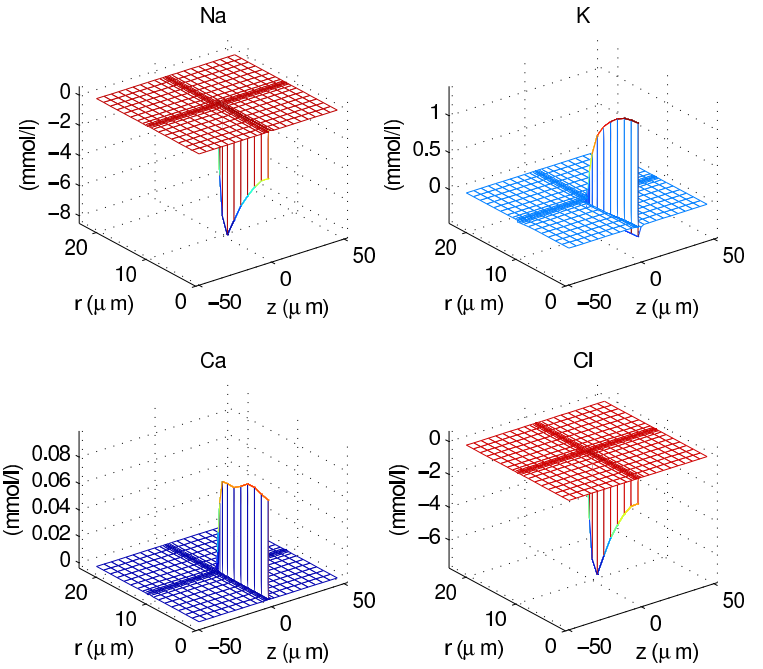


**Figure 8.** The cumulative *change* in ionic concentrations from the initial value, in the cardiac simulation with variable mesh width. The plot of the cumulative concentration changes of $Na^+$, $K^+$ and $Cl^-$ at $t = 2$ ms shown. As with the previous figure, the radial cross section is plotted. The mesh size is $N_z \times N_r = 48 \times 32$ in this computation. Concentrations are in mmol/l and lengths in $\mu$m.

*Convergence in space.* As we remarked above, the gap width $l_g$ is four orders of magnitude smaller than the cell length $l_A$. We therefore use a nonuniform mesh, both in the axial and radial directions.

In the axial direction, we lay a mesh whose width is of order $l_g/2^n$ when $-l_g/2 < z < l_g/2$ and of order $l_A/n$ away from the gap where $z \sim \pm(l_A/2)$, where $n$ is the number of steps in each direction into which the lengths of our system are divided. For meshes in between, we interpolate the two widths with an approximate geometric sequence. In the radial direction, we lay a mesh of width of order $l_g$ near $r = l$ and of order $l$ where $r = l \pm l$. Again, we interpolate between the extremes with an approximate geometric sequence. We give details of this construction below.

We first define a function $f$ on $0 \le z \le (l_A + l_g)/2$:

$$f(z) = \begin{cases} 2z/l_g & \text{if } 0 \le z \le l_g/2, \\ (2/(l_g b))\log\bigl(1 + b(z - l_g/2)\bigr) + 1 & \text{if } l_g/2 \le z \le z_\beta, \\ ((n_z - 1)/l_A)(z - l_A/2) + n_z & \text{if } z_\beta \le z \le l_A/2, \end{cases} \tag{64}$$

where $n_z$ is an integer parameter that we specify, and $b$ and $z_\beta$ are determined so that $f$ is continuously differentiable at $z = z_\beta$. We define the FV boundaries $z_k$ using $f(z)$ as follows:

$$z_k = f^{-1}\Big(\frac{n_z}{N_z/2}k\Big), \quad k = 0, \ldots, N_z/2, \tag{65}$$

where $N_z/2$ is a multiple of $n_z$. This construction adjusts the FV width depending on whether the location is far away from the intercellular gap. For $z < 0$, we take the FV boundaries to be the reflection of the $z_k$ above with respect to $z = 0$.

In the radial direction, we shall take the following mesh. We first define the following function $g$ analogous to $f$ above. For $r > l$ let

$$g(r) = \begin{cases} (2/(l_g b))\log(1 + b(r - l)) & \text{if } l \le r \le r_\beta, \\ (n_r/2l)(r - l) + n_r & \text{if } r_\beta \le r \le 2l, \end{cases} \tag{66}$$

where $n_r$ is an integer parameter that we specify, and $b$ and $r_\beta$ are determined so that $g$ is continuously differentiable at $r = r_\beta$. We define the FV boundaries $r_k$ using $g(r)$ as follows:

$$r_k = g^{-1}\Big(\frac{n_r}{N_r/2}k\Big), \quad k = 0, \ldots, N_r/2, \tag{67}$$

where $N_r/2$ is a multiple of $n_r$. For $r < l$, we take the points $2l - r_k$ as the FV boundaries. This construction again has the benefit of concentrating the meshes toward the membranes and near the gaps.

The coarsest level starts with 2 meshes $-l_g/2 < z < l_g/2$ and 5 meshes each for $z < -l_g/2$ and $z > l_g/2$, a total of $N_z = 12$ meshes in the axial direction. This corresponds to $n_z = 6$ in (64). In the radial direction, the coarsest level is $N_r = 8$ meshes, which corresponds to $n_r = 4$ in (66). We take

$$N_r = 32 \times 2^{n-1}, \quad N_z = 48 \times 2^{n-1}, \quad \Delta t = 0.02\,\text{ms}, \quad N_T = \frac{T_e}{\Delta t} = 200, \tag{68}$$

where $n = 1, \ldots, 4$.

Spatial convergence is assessed in exactly the same way as in the axonal case. Table 6 lists the rate of convergence for both $c_i$ and $\phi$ at the three diameters with three norms, $L^1$, $L^2$ and $L^\infty$ at $t = 4\,\text{ms}$. Convergence rates at other time points were similar. We see approximate second order convergence overall, similarly to the neuronal axon calculation of Section 7.1.

*Convergence in time.* We vary the time step so that

$$\Delta t = 0.02 \times 2^{1-n}, \quad N_T \equiv \frac{T_e}{\Delta t} = 200 \times 2^{n-1}, \tag{69}$$

where $n = 1, \ldots, 4$. As the spatial mesh, we use $N_r = 64$, $N_z = 96$.

| norm | $r_p^s[c_1, 64]$ | $r_p^s[c_2, 64]$ | $r_p^s[c_3, 64]$ | $r_p^s[c_4, 64]$ | $r_p^s[\phi, 64]$ |
|---|---|---|---|---|---|
| $L^1$ | 1.90 | 1.91 | 1.94 | 1.94 | 2.00 |
| $L^2$ | 1.95 | 1.87 | 1.89 | 1.97 | 2.00 |
| $L^\infty$ | 1.88 | 1.89 | 2.10 | 1.83 | 2.00 |

**Table 6.** Convergence rate in space ($r_p^s$) in the cardiac simulation. Values computed at $t = 4$ ms, and $N_r = 64$.

| norm | $r_p^t[c_1, 400]$ | $r_p^t[c_2, 400]$ | $r_p^t[c_3, 400]$ | $r_p^s[c_4, 400]$ | $r_p^s[\phi, 400]$ |
|---|---|---|---|---|---|
| $L^1$ | 1.01 | 1.02 | 1.03 | 1.02 | 1.06 |
| $L^2$ | 1.02 | 1.02 | 1.03 | 1.02 | 1.07 |
| $L^\infty$ | 1.06 | 1.04 | 1.08 | 1.06 | 1.07 |

**Table 7.** Convergence rate in time ($r_p^t$) in the cardiac simulation. Values computed at $t = 4$ ms, and $N_T = 400$.

Table 7 lists the rate of convergence for both $c_i$ and $\phi$ with three norms, $L^1$, $L^2$ and $L^\infty$ at $t = 4$ ms. We see first order convergence for all variables, similarly to the corresponding results in Section 7.1.

*Convergence in space and time.* We vary the time step and spatial mesh so that

$$N_z = 96 \times 2^{n-1}, \quad N_r = 64 \times 2^{n-1}, \quad \Delta t = 0.02 \times 4^{1-n}, \quad N_T \equiv \frac{T_e}{\Delta t} = 200 \times 4^{n-1},$$

where $n = 1, \ldots, 3$. The observed convergence rate in Table 8 is the expected order of two overall similarly to corresponding results in Section 7.1.

| norm | $r_p^{st}[c_1, 64]$ | $r_p^{st}[c_2, 64]$ | $r_p^{st}[c_3, 64]$ | $r_p^{st}[c_4, 64]$ | $r_p^{st}[\phi, 64]$ |
|---|---|---|---|---|---|
| $L^1$ | 2.05 | 2.07 | 2.09 | 2.05 | 2.16 |
| $L^2$ | 2.06 | 2.08 | 2.09 | 2.05 | 2.20 |
| $L^\infty$ | 2.16 | 2.11 | 2.22 | 2.16 | 2.20 |

**Table 8.** Convergence rate in space and time ($r_p^{st}$) in cardiac simulation. Values computed at $t = 4$ ms, and $N_z = 64$, $N_T = 200$.

## 8. General two-dimensional geometry

In this section we consider three examples of general two-dimensional geometry. All three cases involve one or more cells in a two-dimensional square computational domain. Let the computational domain be of size $l$. Take the origin of the domain to be at the center of the computational domain, and take the $x$ and $y$ axes parallel

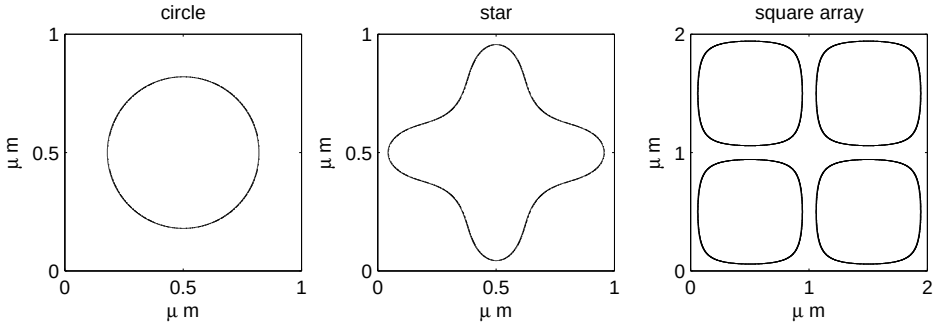


**Figure 9.** Shapes of cells used in computational experiments.

to the sides of the square computational domain. We consider the following three cases as regions of the intracellular domain.

$$\left(\frac{2x}{l}\right)^2 + \left(\frac{2y}{l}\right)^2 < \frac{105}{256}, \quad l = 1\ \mu\text{m},$$

$$\exp\left(-\left(\frac{2x}{l}\right)^2 - 10y\right) + \exp\left(-\left(\frac{2y}{l}\right)^2 - 10x\right) > \frac{1}{2}, \quad l = 1\ \mu\text{m},$$

$$\sin^2\frac{4\pi x}{l}\sin^2\frac{4\pi y}{l} > \frac{1}{30}, \quad l = 2\ \mu\text{m}.$$

The first represents a circular cell, the second a star-shaped cell and the third represents four intracellular domains in a $2 \times 2$ square array (Figure 9).

We use parameter values that are as close as possible to physiological parameters in the context of a two-dimensional geometry. The value of $l$ is chosen so that it is a typical scale for microstructures in the central nervous system[18; 15; 30]. For the ionic channel model, we use the Hodgkin–Huxley kinetics. Given the geometries are two-dimensional, we cannot claim that our geometries correspond closely to those of specific physiological systems. However, even our two dimensional studies may be of physiological interest as the cross-sectional profile of systems with large longitudinal extent. For example, adjacent axons that run parallel may influence the electrical activity of one another. Such coupling has been implicated in neuropathic pain [12] and has been suggested to play a role in the corpus callosum and optic and auditory nerves [33]. The square array example above may be seen as a cross section of four axons running parallel.

At the outer boundary of the computational domain, we impose either no-flux or Dirichlet boundary conditions. In the case of Dirichlet boundary conditions, we set the $c_i$ to be equal to their initial values, and we set $\phi$ equal to 0. If we can demonstrate that the scheme performs well under no-flux and Dirichlet boundary conditions, it would then seem likely that the scheme will perform well for mixed boundary conditions.

| | | |
|---|---|---|
| $T$ | Absolute temperature | $273.15+37$ K |
| $D_{Na^+}$ | Diffusion coefficient of $Na^+$ | $0.266\ \mu m^2/ms$ |
| $D_{K^+}$ | Diffusion coefficient of $K^+$ | $0.392\ \mu m^2/ms$ |
| $D_{Cl^-}$ | Diffusion coefficient of $Cl^-$ | $0.406\ \mu m^2/ms$ |
| $c^{int}_{Na^+}\big\vert_{t=0}$ | Initial intracellular concentration of $Na^+$ | 10 mmol/l |
| $c^{ext}_{Na^+}\big\vert_{t=0}$ | Initial extracellular concentration of $Na^+$ | 145 mmol/l |
| $c^{int}_{K^+}\big\vert_{t=0}$ | Initial intracellular concentration of $K^+$ | 140 mmol/l |
| $c^{ext}_{K^+}\big\vert_{t=0}$ | Initial extracellular concentration of $K^+$ | 5 mmol/l |
| $c^{int}_{Cl^-}\big\vert_{t=0}$ | Initial intracellular concentration of $Cl^-$ | 20 mmol/l |
| $c^{ext}_{Cl^-}\big\vert_{t=0}$ | Initial extracellular concentration of $Cl^-$ | 150 mmol/l |
| $\phi_m\vert_{t=0}$ | Initial transmembrane potential, $\phi^{int}-\phi^{ext}$ | $-70$ mV |
| $G_{Na}$ | Maximal $Na^+$ channel conductance | $600\ mS/cm^2$ |
| $G_K$ | Maximal $K^+$ channel conductance | $180\ mS/cm^2$ |
| $G_L$ | Leak conductance (carried by $K^+$ ions) | $1.5\ mS/cm^2$ |

**Table 9.** Parameter values used in the simulation for general two-dimensional geometries.

In order to observe appreciable changes in ionic concentrations over the time range of the computational study, we scaled the maximal conductances by a factor of 5 and decreased the diffusion coefficient by a factor of 5 with respect to the values of Table 1. The ionic makeup of the simulation is therefore $Na^+$, $K^+$ and $Cl^-$, where the concentrations and the diffusion coefficients used are summarized in Table 9. As before, the immobile charge density is initialized so that electroneutrality is strictly satisfied at $t = 0$. We initialize $\lambda_i$ with $\tilde{\lambda}_i$ evaluated using the initial concentrations and membrane potential.

We add the following the membrane conductances for $0 \le t \le \tau_e$ to initiate an action potential for each of the three geometries.

$$G^{add}_{Cl^-} = G^{add}_{Na^+} = G^{add}_{K^+} = \begin{cases} 200\left(\dfrac{2y}{l}\right)^2\left(1-\cos\dfrac{2\pi t}{\tau_e}\right) & \text{if } y<0,\ t<\tau_e = 1\text{ ms},\\ 0 & \text{otherwise.}\end{cases}$$

We run the simulation for a total of $T_e = 2$ ms. Snapshots from the simulation are given in Figures 10–12, where a no-flux boundary condition is used at the boundary of the computational domain.

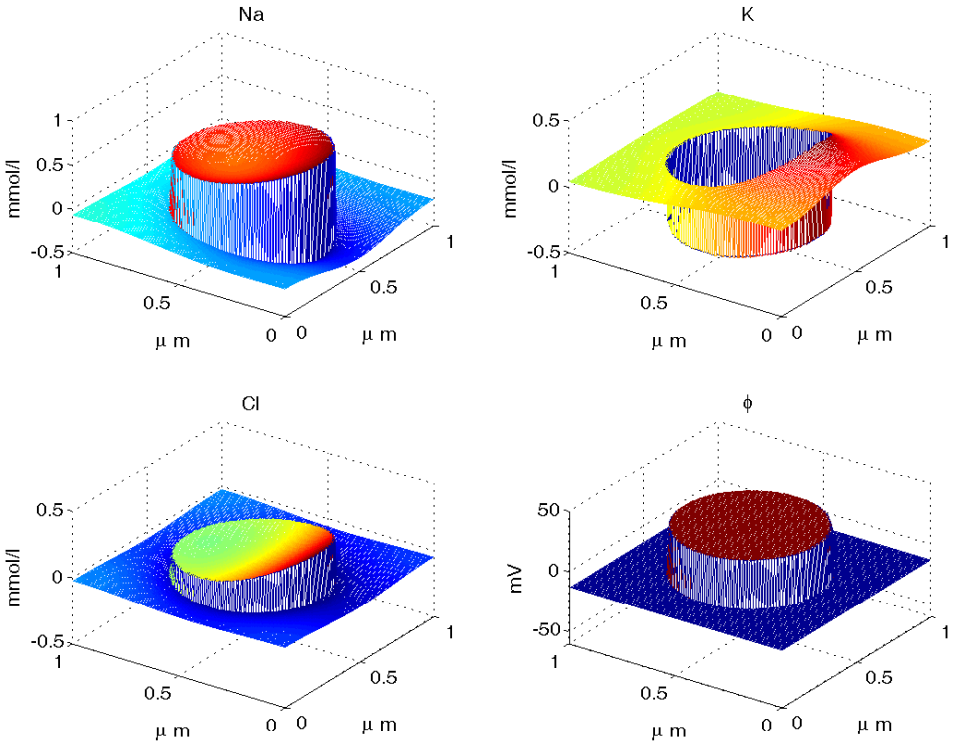


**Figure 10.** Circular geometry: cumulative change in ionic concentrations and electrostatic potential $\phi$ computed under no-flux boundary conditions at the outer boundary of the computational domain. Snapshot at $t = 0.6$ ms. Mesh size: $128 \times 128$.

**8.1.** ***Convergence in space.*** We lay a uniform mesh of $N_x \times N_x$ over the computational domain, where the membrane cuts through the uniform mesh as described in the above. We vary $N_x$ in multiples of 2. We take

$$N_x = 32 \times 2^{n-1}, \quad \Delta t = 0.02\,\text{ms}, \quad N_T = T_e/\Delta t = 100, \tag{70}$$

where $n = 1, \ldots, 5$. Convergence is measured similarly to the cylindrical cases discussed above.

We tabulate the convergence rates in Table 10. We see that it is linear to supralinear. For $\phi$, the rate of convergence is not smooth as the mesh is refined (see Figure 13 on page 125). Given that we observe smooth second order convergence in the case of cylindrical geometry, we infer that this behavior arises because the Cartesian cells are randomly cut by the membrane as the mesh is refined. A direction for future study would be to improve the discretization of the equations near the membrane or adopt a better discretization of the geometry to improve the convergence profile.

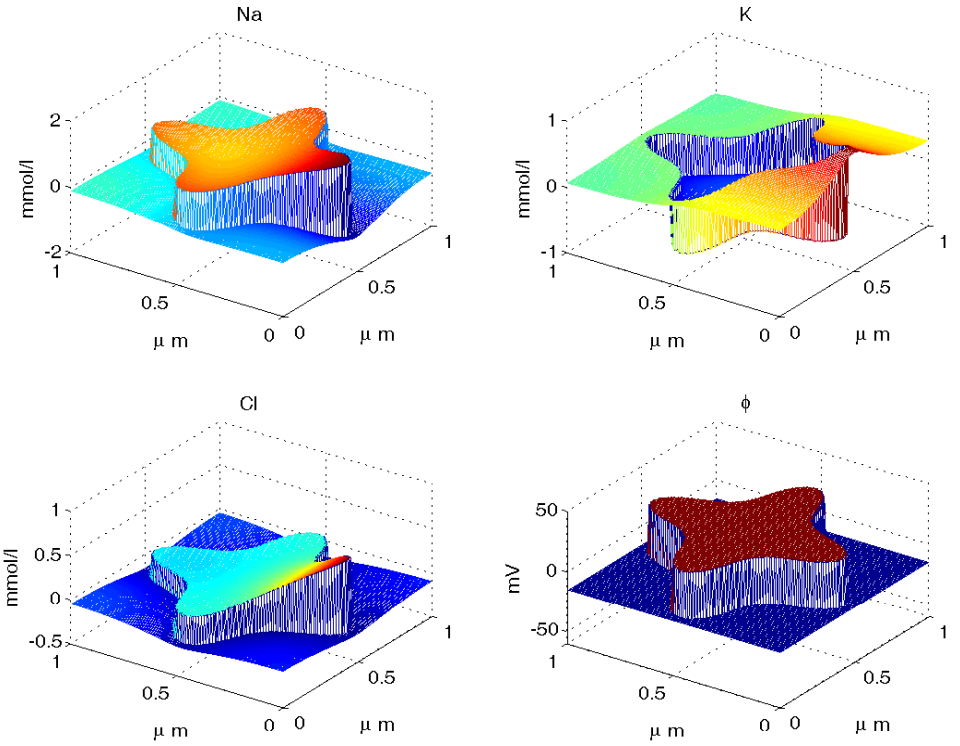


**Figure 11.** Star geometry: cumulative change in ionic concentrations and electrostatic potential $\phi$ computed under no-flux boundary conditions at the outer boundary of the computational domain. Snapshot at $t = 0.6$ ms. Mesh size: $128 \times 128$.

| Geometry and norm | | No Flux $c_1$ | No Flux $c_2$ | No Flux $c_3$ | No Flux $\phi$ | Dirichlet $c_1$ | Dirichlet $c_2$ | Dirichlet $c_3$ | Dirichlet $\phi$ |
|---|---|---|---|---|---|---|---|---|---|
| Circle | $L^1$ | 1.52 | 1.54 | 1.51 | 1.50 | 1.07 | 1.04 | 1.15 | 2.24 |
| | $L^2$ | 1.49 | 1.52 | 1.51 | 1.50 | 1.02 | 1.01 | 1.14 | 2.25 |
| | $L^\infty$ | 0.92 | 1.02 | 1.48 | 1.50 | 0.94 | 1.02 | 1.23 | 2.21 |
| Star | $L^1$ | 0.83 | 1.23 | 1.73 | 2.76 | 1.24 | 1.18 | 1.14 | 1.87 |
| | $L^2$ | 1.27 | 1.38 | 1.79 | 2.77 | 1.05 | 1.04 | 1.05 | 1.87 |
| | $L^\infty$ | 1.16 | 1.12 | 1.51 | 2.47 | 1.14 | 1.12 | 0.97 | 1.86 |
| Square Array | $L^1$ | 2.01 | 2.02 | 1.54 | 1.79 | 1.13 | 1.11 | 1.22 | 1.11 |
| | $L^2$ | 1.71 | 1.84 | 1.58 | 1.82 | 1.05 | 1.05 | 1.07 | 1.10 |
| | $L^\infty$ | 0.80 | 0.78 | 0.76 | 1.61 | 0.96 | 1.01 | 1.01 | 1.10 |

**Table 10.** Convergence rate in space ($r_p^s$). Computed at $t = 2$ ms, and $N_x = 128$.

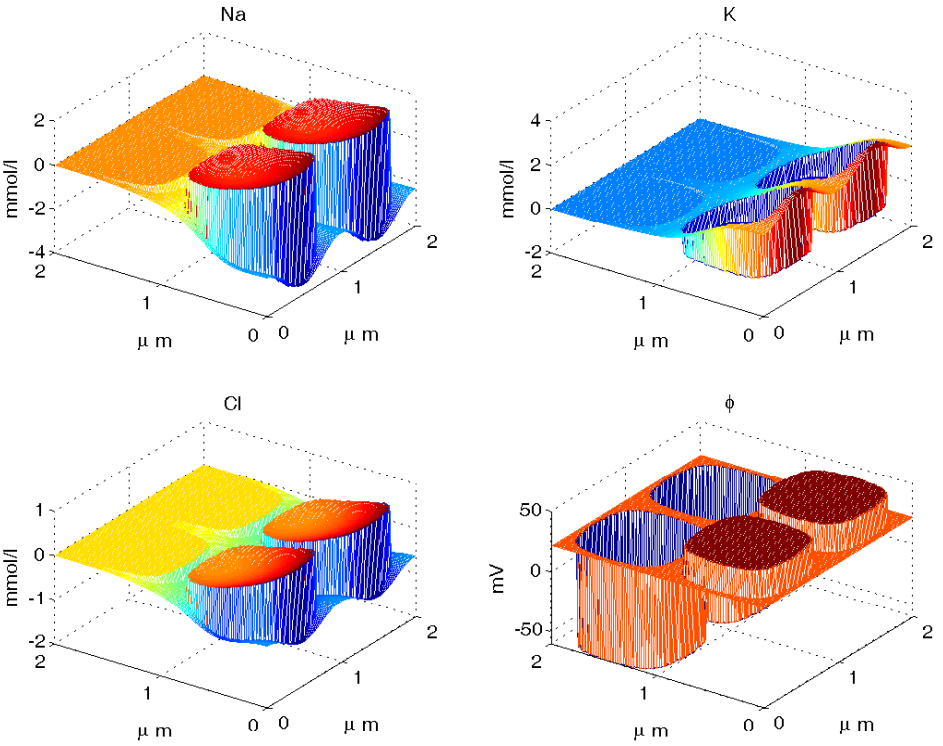


**Figure 12.** Square array geometry: cumulative change in ionic concentrations and electrostatic potential $\phi$ computed under no-flux boundary conditions at the outer boundary of the computational domain. Snapshot at $t = 0.6$ ms. Mesh size: $128 \times 128$.

| Geometry and norm | | No Flux $c_1$ | No Flux $c_2$ | No Flux $c_3$ | No Flux $\phi$ | Dirichlet $c_1$ | Dirichlet $c_2$ | Dirichlet $c_3$ | Dirichlet $\phi$ |
|---|---|---|---|---|---|---|---|---|---|
| Circle | $L^1$ | 1.00 | 1.00 | 0.99 | 1.00 | 1.00 | 1.00 | 1.00 | 1.00 |
| | $L^2$ | 1.00 | 1.00 | 0.99 | 1.00 | 1.00 | 1.00 | 0.99 | 1.00 |
| | $L^\infty$ | 1.00 | 1.01 | 0.69 | 1.00 | 1.00 | 1.01 | 1.00 | 1.00 |
| Star | $L^1$ | 1.00 | 1.00 | 0.99 | 1.00 | 1.00 | 1.00 | 0.99 | 1.00 |
| | $L^2$ | 1.00 | 1.00 | 0.99 | 1.00 | 1.00 | 1.00 | 0.99 | 1.00 |
| | $L^\infty$ | 1.00 | 0.91 | 0.86 | 1.00 | 1.00 | 0.91 | 0.86 | 0.99 |
| Square Array | $L^1$ | 0.99 | 0.99 | 0.98 | 1.00 | 0.99 | 0.99 | 0.98 | 0.99 |
| | $L^2$ | 0.99 | 0.99 | 0.98 | 1.00 | 0.99 | 0.99 | 0.97 | 0.99 |
| | $L^\infty$ | 0.99 | 0.99 | 1.08 | 1.00 | 0.99 | 0.82 | 0.95 | 0.99 |

**Table 11.** Convergence rates in time ($r_p^t$). Computed at $t = 2$ ms, and $N_T = 200$.

**8.2.** ***Convergence in time.*** For convergence in time, we let

$$\Delta t = 0.04 \times 2^{1-n}\text{ms}, \quad N_T = \frac{T_e}{\Delta t} = 50 \times 2^{n-1}, \tag{71}$$

where $n = 1, \ldots, 5$. For the spatial grid, we take $N_x = 64$. We give a table of the convergence rates in Table 11. We see first order convergence in all cases.

**8.3.** ***Convergence in space and time.*** We test convergence in space and time. As was demonstrated above, convergence in space is linear to supralinear. We thus refine the time step proportionally to the spatial step in order to study spatiotemporal convergence. We expect to see first order convergence in this case. We let

$$\Delta t = 0.04 \times 2^{1-n}\text{ms}, \quad N_T = \frac{T_e}{\Delta t} = 50 \times 2^{n-1}, \quad N_x = 64 \times 2^{n-1}, \tag{72}$$

where $n = 1, \ldots, 4$. We give a table of the convergence rates in Table 12. We observe approximate first order convergence in all cases as expected.

| Geometry and norm | | No Flux $c_1$ | No Flux $c_2$ | No Flux $c_3$ | No Flux $\phi$ | Dirichlet $c_1$ | Dirichlet $c_2$ | Dirichlet $c_3$ | Dirichlet $\phi$ |
|---|---|---|---|---|---|---|---|---|---|
| Circle | $L^1$ | 1.01 | 1.01 | 1.01 | 1.01 | 1.00 | 1.00 | 1.02 | 1.00 |
| | $L^2$ | 1.01 | 1.01 | 1.01 | 1.01 | 1.01 | 1.01 | 1.01 | 1.00 |
| | $L^\infty$ | 1.00 | 1.01 | 1.01 | 1.01 | 1.00 | 1.01 | 1.01 | 1.00 |
| Star | $L^1$ | 0.99 | 1.00 | 0.92 | 1.00 | 0.99 | 0.99 | 0.93 | 0.99 |
| | $L^2$ | 0.99 | 0.99 | 0.92 | 1.00 | 0.99 | 0.99 | 0.92 | 0.99 |
| | $L^\infty$ | 0.98 | 0.99 | 0.93 | 1.00 | 0.98 | 0.99 | 0.93 | 0.99 |
| Square Array | $L^1$ | 0.98 | 0.99 | 0.94 | 0.99 | 0.97 | 0.98 | 0.94 | 0.99 |
| | $L^2$ | 0.98 | 0.99 | 0.94 | 1.00 | 0.97 | 0.98 | 0.94 | 0.99 |
| | $L^\infty$ | 0.99 | 1.01 | 0.94 | 0.99 | 0.96 | 0.97 | 0.96 | 0.99 |

**Table 12.** Convergence rates in space and time $r_p^{st}$. Computed at $t = 2$ ms, and $Nx = 128$, $N_T = 100$.

## 9. Conclusion

We have presented a numerical method for an electrodiffusion model of cellular electrical activity, which we call the electroneutral model. The ionic concentrations $c_i$ obey the drift diffusion equations and the electrostatic potential $\phi$ evolves so as to ensure electroneutrality. The boundary conditions at the membrane are expressed in terms of the capacitive current term $C_\text{m}((\partial\phi_\text{m})/(\partial t))$ as well as the ionic channel current term $j_i$. We have a system of partial differential equations satisfied in both

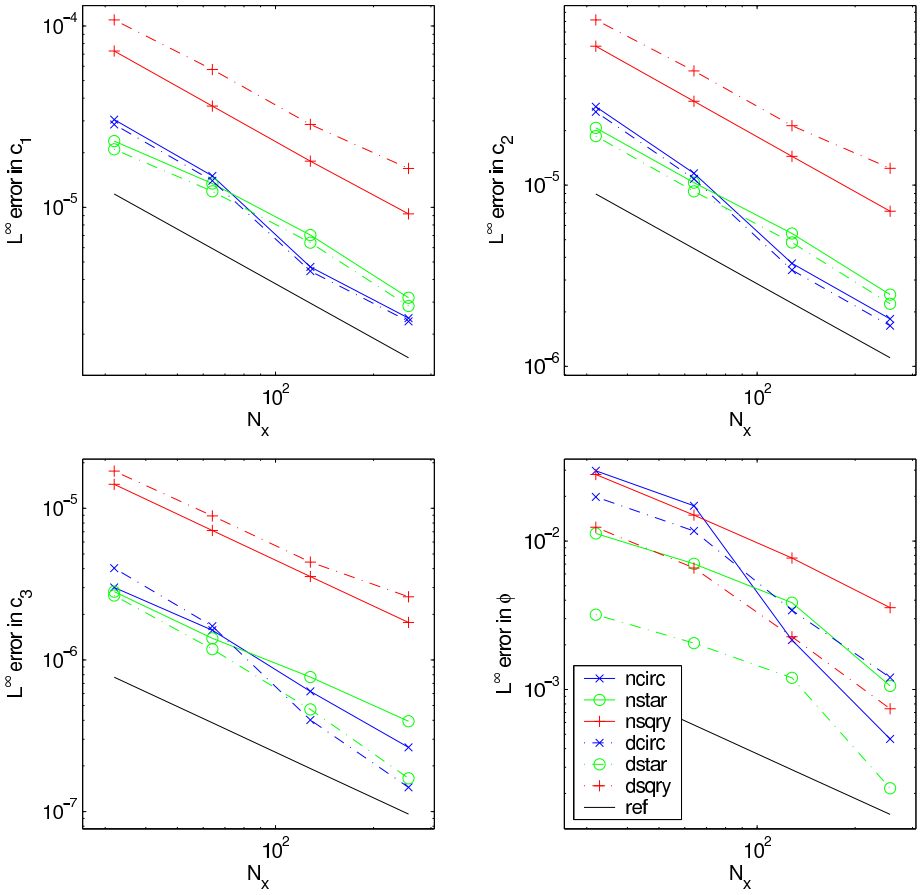


**Figure 13.** $L^\infty$ error in space for $c_i$(mmol/l) and $\phi$(mV). Error measured at 2 ms. ncirc, dcirc: circular geometry with no-flux/Dirichlet boundary conditions; nstar; dstar: star geometry; nsqry, dsqry: square array geometry; ref: reference line indicating first order convergence.

the intracellular and extracellular regions supplemented with nonlinear evolutionary interface conditions at the membrane.

We use a finite volume method in space, a natural discretization since all equations can be written in conservation form. We develop code for both cylindrical and general two dimensional membrane geometries. In the latter case, we use an embedded boundary method, in which the membrane cuts through a regular Cartesian mesh.

The model possesses two diffusive time scales, one that originates from the "diffusion" of the membrane potential and the other from the physical diffusion

of ions. The membrane potential "diffusion" is fast compared to the time scale of biophysical phenomena of interest. We thus develop an implicit scheme to overcome this severe time step restriction that an explicit scheme would face as a result of this disparity of time scales. This means in particular that we must solve an elliptic interface problem where the jump in $\phi$ is not known a priori. The resulting nonlinear algebraic equations in $c_i$ and $\phi$ are solved using an iterative scheme. We fix $c_i$ and solve for $\phi$, and fix $\phi$ to solve for $c_i$. This reduces each linear algebra task to the solution of a symmetric positive definite system. We use either a direct solver or a conjugate gradient iteration to solve these linear systems.

We examined the convergence properties of our scheme in both the cylindrical case and also in the case of the scheme for general two-dimensional geometry. In the cylindrical case, we applied the method to the Hodgkin–Huxley axon and to a model of cardiac action potential propagation. We observe close to second order accuracy in space and first order accuracy in time. For general two dimensional geometries, we test convergence with three geometries in which realistic biophysical parameters are used. We see first order accuracy in time. In space, the convergence rate is linear to supralinear, although in some cases, the convergence profile seems to be somewhat erratic. Improving both the order and the profile of spatial convergence is a direction for future research. We would also like to improve the accuracy of our time stepping scheme. We have employed an operator-splitting framework in which the gating variables defined on the membrane and the electrostatic potential/ionic concentrations defined in the bulk are marched alternately, each of which are discretized using a backward Euler type scheme. Merely replacing the backward Euler scheme with a second order L-stable method will not yield a second order scheme, since the splitting errors incurred will still be first order in time. One future direction would be to adapt splitting methods developed, for example, in [6] to develop higher order time marching schemes.

We anticipate many applications for the numerical scheme introduced in this paper. These include any situation in electrophysiology in which detailed membrane geometry and/or local changes in ionic concentrations are important. One such application was already used as a test problem in this paper. It concerns the transmission of the cardiac action potential across the narrow gap that separates the ends of adjacent myocytes. This gap is normally spanned by specialized channels known as gap junctions [1], but we study here the transmission that can occur even in the absence of these direct connections between neighboring cells [35]. A detailed study of this issue using the present model can be found in [26].

Potential applications in neuroscience include specialized synapses where geometrical relationships, localized extracellular currents, and ionic concentration changes in restricted spaces are thought to play a role [18; 34]. An example of this would be the ribbon synapse of the retina, in which horizontal cells mediate the

interaction between photoreceptors and bipolar cells in ways that are only partly understood [14]. Yet another potential arena of application concerns intracellular electrophysiology, that is, the role of electrodiffusion of ions in the function of such intracellular organelles as the sarcoplasmic reticulum or the mitochondrion.

Most of the applications discussed above will probably require for their full realization a three-dimensional generalization of the code for general two-dimensional geometry that we have developed for the purpose of testing the basic methodology in the present paper. Local mesh refinement will most likely be needed to accommodate the different spatial scales that will interact in any particular application. The principles on which our two-dimensional method are based extend readily to the three-dimensional case even with local mesh refinement. There are, however, significant implementation difficulties that must be overcome, most notably in the representation of the complicated three-dimensional membrane geometry and its interaction with a locally refined mesh. Parallel implementation and efficient solvers will also be needed in the three-dimensional case. This substantial research effort will be rewarded by the ability to make detailed simulations of electrically active cells at a level that takes into account their intricate and beautiful microscopic anatomy.

## Appendix

**A.1.** ***Derivation of*** $\tilde{\lambda}_i^{(k)}$**.** We give a derivation of the expression for $\tilde{\lambda}_i^{(k)}$ in (8). What is presented here is an adaptation of a calculation contained in [27]. For a derivation using matched asymptotics we refer to [25] and [24].

We take a closer look at what is happening in the space charge layer, the thin layers of electric charge accumulation that form on both sides of the membrane. We now derive the ionic composition of the space charge layer when it is in equilibrium with the bulk solution in the immediate vicinity of the space charge layer.

Our starting point is the following Poisson–Nernst–Planck system satisfied in both the intracellular and extracellular regions.

$$\frac{\partial c_i}{\partial t} = -\nabla \cdot \boldsymbol{f}_i, \tag{73}$$

$$\boldsymbol{f}_i = -D_i\left(\nabla c_i + \frac{q z_i c_i}{k_B T}\nabla\phi\right), \tag{74}$$

$$-\epsilon\,\Delta\phi = \rho_0 + \sum_{i=1}^{N} q z_i c_i\,. \tag{75}$$

All quantities except for the dielectric constant $\epsilon$ have been introduced in (1)–(3). Instead of the electroneutrality condition (3), we have the Poisson equation (75). Taking $c_0$ and $L_0$ to be the representative ionic concentration and spatial scales

respectively, the Poisson equation can be nondimensionalized as

$$-\left(\frac{r_d}{L_0}\right)^2 \tilde{\Delta}\tilde{\phi} = \tilde{\rho_0} + \sum_{i=1}^{N} z_i \tilde{c}_i, \tag{76}$$

where $\tilde{\cdot}$ denote the respective nondimensionalized quantities and operators. In (76) $r_d$ is the Debye length given by

$$r_d = \sqrt{\frac{\epsilon k_B T}{q^2 c_0}}. \tag{77}$$

Given that $r_d \approx 1$ nm and $L_0$ is on the order or $\mu$m to cm in biophysical systems, $(r_d/L_0)^2$ is a very small quantity. We may thus safely disregard the left hand side of (76) provided we are sufficiently far away from the membrane. This amounts to taking the right hand side of (75) to be equal to 0. This leads to the electroneutrality condition (3). However close to the membrane we have a boundary layer of thickness $\mathbb{O}(r_d)$, within which the ionic concentrations deviate from electroneutrality. In this space charge layer, we must deal with the Poisson–Nernst–Planck system (73), (74) and (75).

We make some assumptions in our analysis of the space charge layer. We suppose that the quantities within the space charge layer experience fast spatial variation in the direction normal to the membrane but slow spatial variation in the direction parallel to the membrane. Under this "boundary layer" assumption, all quantities may be treated as functions only of the distance from the membrane. This also implies that the ionic fluxes must be equal to 0 to leading order within the space charge layer. It is possible to formalize this argument within the traditional framework of matched asymptotics as presented in [25] and [24]. We also make the assumption that the deviation of the electrostatic potential and hence the ionic concentration from its bulk values is small. This assumption is justified because the membrane capacitance is "small" in biophysical systems. For a further elaboration of this point we refer the reader to [27].

Let $x$ denote the distance coordinate normal to the membrane surface. Then, according to the assumptions just stated, (73)–(75) become

$$0 = -D_i\left(\frac{\partial c_i}{\partial x} + \frac{q z_i c_i}{k_B T}\frac{\partial \phi}{\partial x}\right), \tag{78}$$

$$-\frac{\partial^2 \phi}{\partial x^2} = \frac{1}{\epsilon}\left(\rho_0 + \sum_{i=1}^{N} q z_i c_i\right), \tag{79}$$

which hold on $0 < x < \infty$ with $c_i(\infty)$ and $\phi(\infty)$ given. Here, $x = 0$ is the intracellular or extracellular face of the membrane, and $x = \infty$ corresponds to the bulk solution where $c_i$ and $\phi$ values in the space charge layer are to be matched

with the bulk values. For now we shall assume that $c_i(\infty)$ and $\phi(\infty)$ are constant in time. Assuming that the background fixed charge density $\rho_0$ varies on the scale of the cellular size $L_0$, its variation within the thickness of the space charge layer is negligible, of order $\mathbb{O}(r_d/L_0)$. Thus, we will treat $\rho_0$ as being constant within the space charge layer. It is important to note that these values at $x = \infty$ satisfy electroneutrality, that is,

$$\rho_0 + \sum_{i=1}^{N} q z_i c_i(\infty) = 0. \tag{80}$$

Equation (78) can be integrated easily to obtain,

$$c_i(x) = c_i(\infty) \exp\Big(-\frac{q z_i}{k_B T}(\phi(x) - \phi(\infty))\Big). \tag{81}$$

We substitute this into (79) to find,

$$-\frac{\partial^2 \phi}{\partial x^2} = \frac{1}{\epsilon}\left(\rho_0 + \sum_{i=1}^{N} q z_i c_i(\infty) \exp\Big(-\frac{q z_i}{k_B T}(\phi(x) - \phi(\infty))\Big)\right). \tag{82}$$

We now assume, as we stated earlier, that the deviation of the electrostatic potential within the space charge layer from the bulk value is small.

$$\left|\frac{q z_i}{k_B T}(\phi(x) - \phi(\infty))\right| \ll 1. \tag{83}$$

Then, taking into account the electroneutrality condition at $x = \infty$ (80), we obtain

$$c_i(x) = c_i(\infty)\Big(1 - \frac{q z_i}{k_B T}(\phi(x) - \phi(\infty))\Big) \tag{84}$$

and

$$\frac{\partial^2}{\partial x^2}(\phi(x) - \phi(\infty)) = \gamma^2(\phi(x) - \phi(\infty)),$$

where

$$\gamma^2 = \sum_{i=1}^{N} \frac{(q z_i)^2 c_i(\infty)}{\epsilon k_B T}. \tag{85}$$

Letting $\gamma$ be the positive square root of $\gamma^2$ ($1/\gamma$ is nothing other than the Debye length), we find the unique bounded solution

$$\phi(x) - \phi(\infty) = (\phi(0) - \phi(\infty)) \exp(-\gamma x), \tag{86}$$

and hence according to (84),

$$c_i(x) - c_i(\infty) = -c_i(\infty) \frac{q z_i}{k_B T}(\phi(0) - \phi(\infty)) \exp(-\gamma x). \tag{87}$$

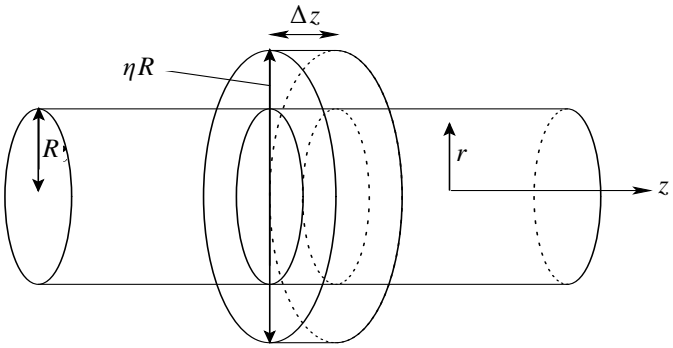


**Figure 14.** Derivation of the cable model. A portion of a cylindrical cell is shown. As explained in the main text, the divergence theorem is applied to the intracellular and extracellular slabs of thickness $\Delta z$, shown above.

Using this equation, we may compute $\sigma_i$ as

$$\sigma_i = \int_0^\infty q z_i (c_i(x) - c_i(\infty)) dx = -c_i(\infty) \frac{(q z_i)^2}{k_B T \gamma} (\phi(0) - \phi(\infty)). \tag{88}$$

Using the above and noting that $\sum_{i=1}^N \sigma_i = \sigma$, we immediately obtain

$$\sigma_i = \frac{z_i^2 c_i(\infty)}{\sum_{i'=1}^N z_{i'}^2 c_{i'}(\infty)} \sigma. \tag{89}$$

The coefficient in front of $\sigma$ corresponds to the expression for $\tilde{\lambda}_i$ in (8).

If the bulk concentrations are not changing in time, the fractional contribution $\sigma_i/\sigma = \lambda_i$ of (8) will be equal to $\tilde{\lambda}_i$. If the bulk concentration changes slowly with time, we expect the ionic concentration profile within the space charge layer to closely follow the corresponding equilibrium profile calculated above, on the diffusive time scale within the space charge layer. We thus let $\lambda_i$ relax to $\tilde{\lambda}_i$ with the time constant $\tau = r_d^2/D_0$, where $D_0$ is the representative magnitude of ionic diffusion coefficient.

**A.2.** ***Derivation of the cable model.*** We give a short derivation of the cable model from (15) and (16). Our derivation here can be formalized using thin domain asymptotics. See [25] and [24] for details.

Suppose the cell is cylindrical in shape (Figure 14). Let $z$ be the axial coordinate and $r$ be the radial coordinate. The membrane is located at $r = R$. The intracellular space corresponds to $r < R$ and the extracellular space to $R < r < \eta R$ where $\eta > 1$ is some constant. Now, consider the cross sectional slab between $z = z_0$ and $z = z_0 + \Delta z$. Let us compute the integral of $\Delta\phi$ over the region $z_0 < z < z_0 + \Delta z$,

$r < R$. We get

$$\int_{z_0<z<z_0+\Delta z, r<R} \Delta\phi\, dV = \int_{z=z_0+\Delta z, r<R} \frac{\partial\phi}{\partial z} dA - \int_{z=z_0, r<R} \frac{\partial\phi}{\partial z} dA + \int_{z_0<z<z_0+\Delta z, r=R} \frac{\partial\phi}{\partial r} dA, \quad (90)$$

where we used the divergence theorem. The symbols $dV$ and $dA$ denote volume and surface integration respectively. Now, note by (17) that $\Delta\phi = 0$. Therefore, the left hand side of (90) is 0, and we have

$$\int_{z=z_0+\Delta z, r<R} \frac{\partial\phi}{\partial z} dA - \int_{z=z_0, r<R} \frac{\partial\phi}{\partial z} dA = -\int_{z_0<z<z_0+\Delta z, r=R} \frac{\partial\phi}{\partial r} dA. \quad (91)$$

Dividing by $\Delta z$ and taking the limit as $\Delta z$ goes to 0, we obtain the following relationship.

$$\frac{\partial}{\partial z}\int_{z=z_0} \frac{\partial\phi}{\partial z} dA = -\int_{z=z_0, r=R} \frac{\partial\phi}{\partial r} d\ell, \quad (92)$$

where $d\ell$ denotes a line integral. Now, we make the assumption that the cylindrical diameter is small so that the electrostatic potential $\phi$ varies very little over the diameter of the cylinder. We thus take the approximation that $\phi = \phi^{\text{int}}(z)$ does not depend on the radial direction in $r < R$. Under this approximation, the above becomes

$$a^{\text{int}} \pi R^2 \frac{\partial^2 \phi^{\text{int}}}{\partial z^2} = \int_{r=R} \left( C_{\text{m}} \frac{\partial \phi_m}{\partial t} + I \right) d\ell, \quad (93)$$

where we used (18). Note that the above is valid for any value of $z_0$, and thus, we have omitted reference to $z_0$. $\phi_m$ is the membrane potential, the difference in $\phi$ across the membrane. $a^{\text{int}}$ is the value of $a$ (which appears in (16) as $a^{(k)}$ and $a^{(l)}$) in the intracellular space.

A similar calculation, applied to the extracellular region $z_0 < z < z_0 + \Delta z$, $R < r < R^{\text{ext}}$, yields

$$a^{\text{ext}} \pi ((\eta R)^2 - R^2) \frac{\partial^2 \phi^{\text{ext}}}{\partial z^2} = -\int_{r=R} \left( C_{\text{m}} \frac{\partial \phi_m}{\partial t} + I \right) d\ell, \quad (94)$$

where we have assumed that $\phi$ in the extracellular region is again, a function only of $z$ and does not depend on the radial direction $r$. Note that the membrane potential $\phi_m$ can now be expressed as $\phi_m = \phi^{\text{int}} - \phi^{\text{ext}}$, and is thus a function only of $z$, and does not depend on the angular coordinate. Rearranging (93) and (94), we may write an equation solely in terms of $\phi_m$:

$$C_{\text{m}} \frac{\partial \phi_m}{\partial t} + \bar{I} = \frac{a^{\text{eff}} R}{2} \frac{\partial^2 \phi_m}{\partial z^2}, \quad a^{\text{eff}} = ((a^{\text{int}})^{-1} + (a^{\text{ext}}(\eta^2 - 1))^{-1})^{-1}. \quad (95)$$

This is nothing other than (20). If we let $a = a^{\text{int}} = a^{\text{ext}}$ and consider the case in which $\eta$ is very large, we may replace $a^{\text{eff}}$ by $a$, as used in (19).

## Acknowledgments

The authors thank Joseph W. Jerome for helpful discussion. Mori was supported by the Henry McCracken and Dissertation Fellowships from New York University, where most of this work was done. Mori also acknowledges support from a MITACS (Mathematics of Information Technology and Complex Systems) team grant (Leah Keshet, PI) and from an NSERC (Natural Sciences and Engineering Research Council) discovery grant (also with Leah Keshet).

## References

[1] D. Aidley, *The physiology of excitable cells*, 4th ed., Cambridge Univ. Press, NY, 1998.

[2] S. Balay, K. Buschelman, W. Gropp, D. Kaushik, M. Knepley, L. McInnes, B. Smith, and H. Zhang, *PETSc Web page*, 2001.

[3] V. Barcilon, J. Cole, and R. Eisenberg, *A singular perturbation analysis of induced electric fields in nerve cells*, SIAM Journal on Applied Mathematics (1971), 339–354. Zbl 0231.92016

[4] O. Bernus, R. Wilders, C. Zemlin, H. Verscelde, and A. Panfilov, *A computationally efficient electrophysiological model of human ventricular cells*, Am. J. Physiol. Heart Circ. Physiol. **282** (2002), 2296–2308.

[5] J. Bockris and A. Reddy, *Modern electrochemistry. Vol. 1, Ionics*, Plenum, 1998.

[6] A. Bourlioux, A. T. Layton, and M. L. Minion, *High-order multi-implicit spectral deferred correction methods for problems of reactive flow*, J. Comput. Phys. **189** (2003), no. 2, 651–675. MR 2004f:76084 Zbl 1061.76053

[7] D. Calhoun and R. J. LeVeque, *A Cartesian grid finite-volume method for the advection-diffusion equation in irregular geometries*, J. Comput. Phys. **157** (2000), no. 1, 143–180. MR 2000k:65166 Zbl 0952.65075

[8] R. Eisenberg and E. Johnson, *Three-dimensional electrical field problems in physiology*, Prog. Biophys. Mol. Biol **20** (1970), no. 1, 1–65.

[9] D. Gutstein, G. Morley, H. Tamaddon, D. Vaidya, M. Schneider, J. Chen, K. Chien, H. Stuhlmann, and G. Fishman, *Conduction slowing and sudden arrhythmic death in mice with cardiac-restricted inactivation of connexin 43*, Circulation Research **88** (2001), no. 8, 333–339.

[10] B. Hille, *Ion channels of excitable membranes*, 3rd ed., Sinauer Associates, 2001.

[11] A. Hodgkin and A. Huxley, *A quantitative description of the membrane current and its application to conduction and excitation in nerve*, Journal of Physiology **117** (1952), 500–544.

[12] J. Jeffreys, *Nonsynaptic modulation of neuronal activity in the brain: electric currents and extracellular ions*, Physiological Reviews **75** (1995), 689–723.

[13] H. Johansen and P. Colella, *A Cartesian grid embedded boundary method for Poisson's equation on irregular domains*, J. Comput. Phys. **147** (1998), no. 1, 60–85. MR 99m:65231 Zbl 0923.65079

[14] M. Kamermans, I. Fahrenfort, K. Schultz, U. Janssen-Bienhold, T. Sjoerdsma, and R. Weiler, *Hemichannel-mediated inhibition in the outer retina*, Science **292** (2001), no. 5519, 1178–1180.

[15] E. Kandel, J. Schwartz, and T. Jessel, *Principles of neural science*, 4th ed., McGraw-Hill/Appleton & Lange, NY, 2000.

[16] J. Keener and J. Sneyd, *Mathematical physiology*, Interdisciplinary Applied Mathematics, no. 8, Springer, New York, 1998. MR 2000c:92010 Zbl 0913.92009

[17] D. A. Knoll and D. E. Keyes, *Jacobian-free Newton–Krylov methods: a survey of approaches and applications*, J. Comput. Phys. **193** (2004), no. 2, 357–397. MR 2004j:65066 Zbl 1036.65045

[18] C. Koch, *Biophysics of computation*, Oxford Univ. Press, New York, 1999.

[19] J. Kucera, S. Rohr, and Y. Rudy, *Localization of sodium channels in intercalated disks modulates cardiac conduction*, Circulation Research **91** (2002), no. 12, 1176–82.

[20] L. Lee and R. J. Leveque, *An immersed interface method for incompressible Navier–Stokes equations*, SIAM J. Sci. Comput. **25** (2003), no. 3, 832–856. MR 2005a:65086

[21] R. J. LeVeque, *Finite volume methods for hyperbolic problems*, Cambridge Texts in App. Math., Cambridge University Press, Cambridge, 2002. MR 2003h:65001 Zbl 1010.65040

[22] A. A. Mayo and C. S. Peskin, *An implicit numerical method for fluid dynamics problems with immersed elastic boundaries*, Fluid dynamics in biology, Contemp. Math., no. 141, Amer. Math. Soc., Providence, RI, 1993, pp. 261–277. MR 93k:76132 Zbl 0787.76055

[23] P. McCorquodale, P. Colella, and H. Johansen, *A Cartesian grid embedded boundary method for the heat equation on irregular domains*, J. Comput. Phys. **173** (2001), no. 2, 620–635. MR 2002h:80009 Zbl 0991.65099

[24] Y. Mori, *From three-dimensional electrophysiology to the cable model: an asymptotic study*, 2009, preprint. arXiv 0901.3914

[25] Y. Mori, *A three-dimensional model of cellular electrical activity*, Ph.D. thesis, New York Univ., 2006. Zbl 1129.92038

[26] Y. Mori, G. I. Fishman, and C. S. Peskin, *Ephaptic conduction in a cardiac strand model with 3d electrodiffusion*, Proceedings of the National Academy of Sciences (2008), to appear.

[27] Y. Mori, J. W. Jerome, and C. S. Peskin, *A three-dimensional model of cellular electrical activity*, Bull. Inst. Math. Acad. Sin. (N.S.) **2** (2007), no. 2, 367–390. MR 2008f:92022 Zbl 1129.92038

[28] J. Neu and W. Krassowska, *Homogenization of syncytial tissues*, Critical reviews in biomedical engineering **21** (1993), no. 2, 137–199.

[29] N. Qian and T. Sejnowski, *An electro-diffusion model for computing membrane potentials and ionic concentrations in branching dendrites, spines and axons*, Biol. Cybern. **62** (1989), 1–15.

[30] ———, *When is an inhibitory synapse effective?*, Proc. Natl. Acad. Sci. USA **87** (1990), 8145–8149.

[31] S. Rohr, *Role of gap junctions in the spread of the cardiac action potential*, Cardiovascular Research **62** (2004), 309–322.

[32] I. Rubinstein, *Electro-diffusion of ions*, SIAM Studies in Applied Mathematics, no. 11, Society for Industrial and Applied Mathematics (SIAM), Philadelphia, PA, 1990. MR 91m:78019

[33] A. Scott, *Neuroscience: A mathematical primer*, Springer, New York, 2002. MR 2003i:92001 Zbl 1018.92003

[34] G. M. Shepherd (ed.), *Synaptic organization of the brain*, Oxford University Press, 1997.

[35] N. Sperelakis, *An electric field mechanism for transmission of excitation between myocardial cells*, Circulation Research **91** (2002), 985–987.

[36] H. A. van der Vorst, *Iterative Krylov methods for large linear systems*, Cambridge Monographs on Applied and Computational Mathematics, no. 13, Cambridge University Press, Cambridge, 2003. MR 2005k:65075 Zbl 1023.65027

[37] ———, *Iterative Krylov methods for large linear systems*, Cambridge Monographs on Applied and Computational Mathematics, no. 13, Cambridge University Press, Cambridge, 2003. MR 2005k:65075 Zbl 1023.65027

Received June 20, 2007. Revised June 22, 2009.

YOICHIRO MORI: ymori@umn.edu
*School of Mathematics, University of Minnesota, 206 Church St. SE, Minneapolis, MN 55455-0487, United States*
http://www.math.umn.edu/∼ymori

CHARLES S. PESKIN: peskin@cims.nyu.edu
*Courant Institute of Mathematical Sciences, New York University, 251 Mercer St., New York, NY 10012-1110, United States*